MEMRISTIVE RESPONSES OF JAMMED GRANULAR COPPER ARRAY SENSORS TO MECHANICAL STRESS

THESIS

Gary A. Willey Jr., BS

AFIT-ENP-14-M-44

DEPARTMENT OF THE AIR FORCE
AIR UNIVERSITY

AIR FORCE INSTITUTE OF TECHNOLOGY

Wright-Patterson Air Force Base, Ohio

AFIT-ENP-14-M-44

MEMRISTIVE RESPONSES OF JAMMED GRANULAR COPPER ARRAY
SENSORS TO MECHANICAL STRESS

THESIS

Presented to the Faculty

Department of Engineering Physics

Graduate School of Engineering and Management

Air Force Institute of Technology

Air University

Air Education and Training Command

in Partial Fulfillment of the Requirements for the

Degree of Master of Science

Gary A. Willey Jr., BS

March 2014

AFIT-ENP-14-M-44

MEMRISTIVE RESPONSES OF JAMMED GRANULAR COPPER ARRAY
SENSORS TO MECHANICAL STRESS

Gary A. Willey Jr., BS

Approved:

_____//signed//_____		7 March 2014
Major Timothy W.C. Zens, PhD (Chairman)		Date
_____//signed//_____		7 March 2014
Alex G. Li, PhD (Member)		Date
_____//signed//_____		7 March 2014
Marina B. Ruggles-Wrenn, PhD (Member)		Date

AFIT-ENP-14-M-44

Abstract

A granular memristive device with the end goal of creating a novel system protection device is introduced in a 1-Dimension array. The electromechanical network will lay the groundwork for future 2-Dimensional and 3-Dimensional devices for simultaneous protection from intrusion. Off the shelf copper spheres with diameter of $710 \pm 11\mu m$ were found through nano-indentation measurements to have elastic modulus of 106GPa, and compressive yield strength of 729MPa, these spheres were prepared for test in a 1-Dimensional array device. The arrays' response to mechanical perturbations modeled by Hertz contact mechanics can be monitored by simultaneous electrical measurements across the multiple metal-insulator-metal junctions. A shift in the nonlinear IV trace behavior to lower resistance states is the result of increasing compressive forces. Additionally a relation of breakdown to ohmic conduction of the junctions is found to be -7.6 in units of Volts per Newton per Interface for a 15 minute thermally oxidized sample array of 4 spheres. This granular array can be preset and monitored retaining the ability to recognize mechanical or electrical interference. The ability to have multiple electromechanically characterized chains within a 3-Dimensional volume allows for a complex redundancy in the future system protection circuit.

To Mom and Dad

Acknowledgements

Table of Contents

List of Figures

List of Tables

MEMRISTIVE RESPONSES OF JAMMED GRANULAR COPPER ARRAY SENSORS TO MECHANICAL STRESS

I. Introduction

Motivation

Many system protection technologies are currently in use for the reduction and illegal circulation of materials and sensitive data. However given the rate of technological advancements and an increase in availability to an intruder, these system protection instruments will inevitably allow unwanted and unnoticed detection. There is no universal answer to device intrusion deterrence, that is to say, with enough time in the intruder presence, technologies can be circumvented. Therefore, further research for the application of novel memristive technology is an attempt to keep 'one step ahead' and making unnoticed intrusion as difficult as possible for the aggressor.

Current security is typically comprised of different perimeters when protecting an item of importance within a static location [25]. This can be inclusive of different combinations of security personnel, fences, and buildings that are equipped with separate vibration, infrared, and motion sensors among other sensors available [25]. Defensive security density should also increase with decreasing radius with respect to that which is being protected [25]. When items of value are being transported, this security perimeter is much smaller and more vulnerable to intrusion.

1

A new device with simultaneous programmable thresholds of mechanical and electrical interference imbedded within a relatively new circuit element would provide a significant security level to the item being protected. When considering the addition of a complex output, it can be suggested that such a device would decrease the chances of false positive alarms and ultimately increase threat detection.

Background

Intrusion evident devices are devices in which any physical invasion is obvious to the user; whether it is breaking into device housing, or probing into the system to intercept electrical transmissions. Intrusion resistance is the trait of a device to take action on unwanted intrusion [25]. An intrusion resistant device will generally not allow, or alert as a result of unwanted interference. To be intrusion resistant, a device must be intrusion evident [25].

Solely intrusion evident devices are generally simple and can be found in commercial use devices, such as the water damage sticker on a cell-phone that voids any existing warranty.

Intrusion resistant devices may be comprised of a combination of several simple intrusion evident devices integrated within a monitoring system [25]. Intrusion resistant devices and practices are common with regards to higher and more thorough level of security. An example of such a practice, tests of protective detonation of a device concluded that usable data was recovered from the 1mm sized chip fragments remaining; measures were taken to store any key material with spacing of more than 1mm [24]. This action resists tampering by destruction, resulting in an unusable sized chip fragment.

2

The United States Government, specifically the National Institute for Standards and Technology (NIST) rate devices and software for security. The invasive physical intrusion resistance standard is known as the Federal Information Processing Standards or FIPS 140 [28]. The various levels of FIPS can be applied to different devices, for certification. An example of a lower level would be the operating system on a popular smart phone which has been given FIPS 140-2 Level 1 for physical and software security [2]. An example of a higher level of physical and software security is the Common Access Card (CAC), issued to government employees for computer access; the CAC's hold a FIPS 140-2 Level 3 for physical and software security [10]. Providing even more protection, the first Level 4 (FIPS 140-1) device was the IBM 4758 [25]. This Crypto processor was equipped with serviceable parts such as batteries kept separate from the processor to prevent a maintainer from invasive acts. The processor was incorporated into an opaque epoxy to make evident of any drilling or cutting [25]. The housing also consisted of aluminum shielding and low pass filter to block any signals at the frequency of internal computation [25]. On top of that, an intrusion sensing layer is wrapped around overlapping zig-zag conducting patterns [25]. If any conduction path is broken, indications of forced entrance are obvious.

The subject of this thesis could potentially be incorporated into such a device, replacing one or multiple intrusion evident measures mentioned above.

Research Objectives

The design proposed in this thesis includes a jammed granular memristor system. This granular system acts as an electromechanical network, chains containing multiple

grains which interact with respect to their relative contact areas, respond to electrical excitation depending on the mechanical loading conditions across the network, the response is also dependent on the surface oxide conditions and number of grains present. Copper oxides have been shown by Castle to provide favorable memristive conditions in thermally oxidized planar copper samples [4]. The jammed granular system takes into account a mechanically stressed oxide interface between the copper spherical particles for electronic as well as mechanical perturbations.

The design will ultimately evolve to a 3-Dimensional volume of granules acting as a sensor for intrusion evident applications. Multiple preset arrays throughout a volume should result in a complex device. Figure 1 shows a 2-Dimensional example; this will eventually be extended to the third dimension. Given the many network possibilities paired with memristive behaviors of copper-copper oxide interfaces, a complex obstacle is created potentially preventing mimicking by an intruder. Ellenbroek highlighted static packed grains with higher loading conditions and the resulting force chains throughout a population [32]. Force chains in 2 and 3-Dimension systems can be simplified into multiple single dimension sphere arrays. Thus this thesis lays the groundwork by 1-Dimension array to be applied in the future.
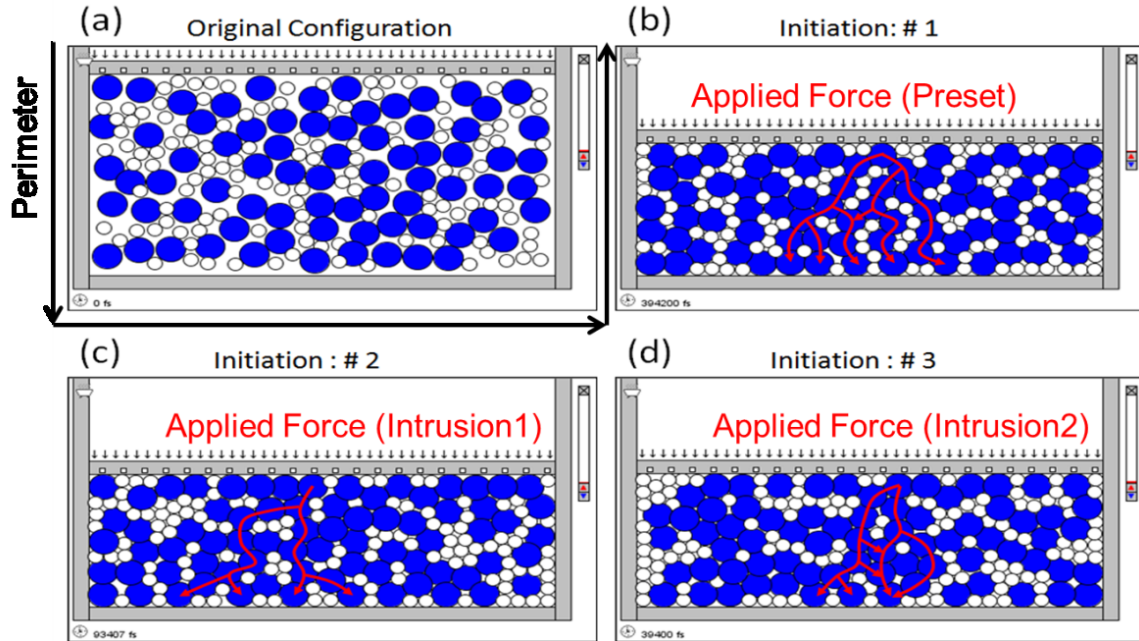
Figure 1: The figure shows a 2D jammed granular system with two sphere types. In this simulation, the blue spheres are conductive while white spheres are insulating. Initial unstressed state (a) shows a random assortment of grains. The images (b) through (d) show various stressed initiations in which different force chains result with each initiation. Image provided by Dr. Alex Li [17].

In the scenario where an intruder does not physically breach a system, but electrically probes it for information, a safe practice is to ensure some degree of noticeable physical intrusion is necessary to reach this point. Designing for the necessity of observable device impingement is the goal in system protection device design. The system protection device proposed in this research allows the user to be aware of not only mechanical invasive actions, but also electrical intrusions by means of this copper granular jammed memristor device. Stand-off detection is possible with this device in that, any mechanical or electrical interference above a predetermined threshold results in a change of electrical properties of the system, measurable by the user. The theory of a

5

memory-resistor (memristor) will be introduced in Chapter 2 of this thesis; in a memristor the current through the device controls its resistance in a nonvolatile nature. Therefore, since changes in the device remain with power loss, the memristive device holds an extra level of redundancy.

The jammed copper granular memristor device is capable of both active and passive monitoring. An active monitoring system would allow the user to be aware of any history of invasive acts and to what degree such actions occurred. A passive configuration of the system could detect the presence of invasive acts above a set threshold with a simple yes or no result. Depending on the configuration, any current flow above a set threshold or change not within predetermined device specifications will cause a resistance switching in the device, thus further investigation can determine if the detection system is actually intruded upon.

Memristors have the trait of distinct current behavior when a voltage sweep is applied; this behavior is in the form of a nonlinear and non-retracing IV plot, commonly known as a hysteresis loop, and shows the device switching from one resistance state to another. Upon the application of a current higher than a threshold, the variable resistance state will switch to a lower resistance state, or in extreme current change instances, a breakdown occurs causing irreversibly ohmic relations; essentially turning the memristor in that specific jammed orientation into a wire. Figure 2 shows examples of a hysteretic IV trace, characteristic of a memristor for both the active and passive intrusion evident cases. In the before intrusion cases, (a) and (b), the device responds similarly, the difference is that in case (b), a threshold resistance is set by the user. For the actively

monitored device after intrusion case (d), the IV trace hysteresis loop shifts to a lower resistance than R_{TH} thus indicating an intrusive force is observed. After intrusion occurs in the passive case, (a) completely ohmic resistance is observed in the after intrusion measurement.

	Passive	Active
Before Intrusion	(a)	(b)
After Intrusion	(c)	(d)
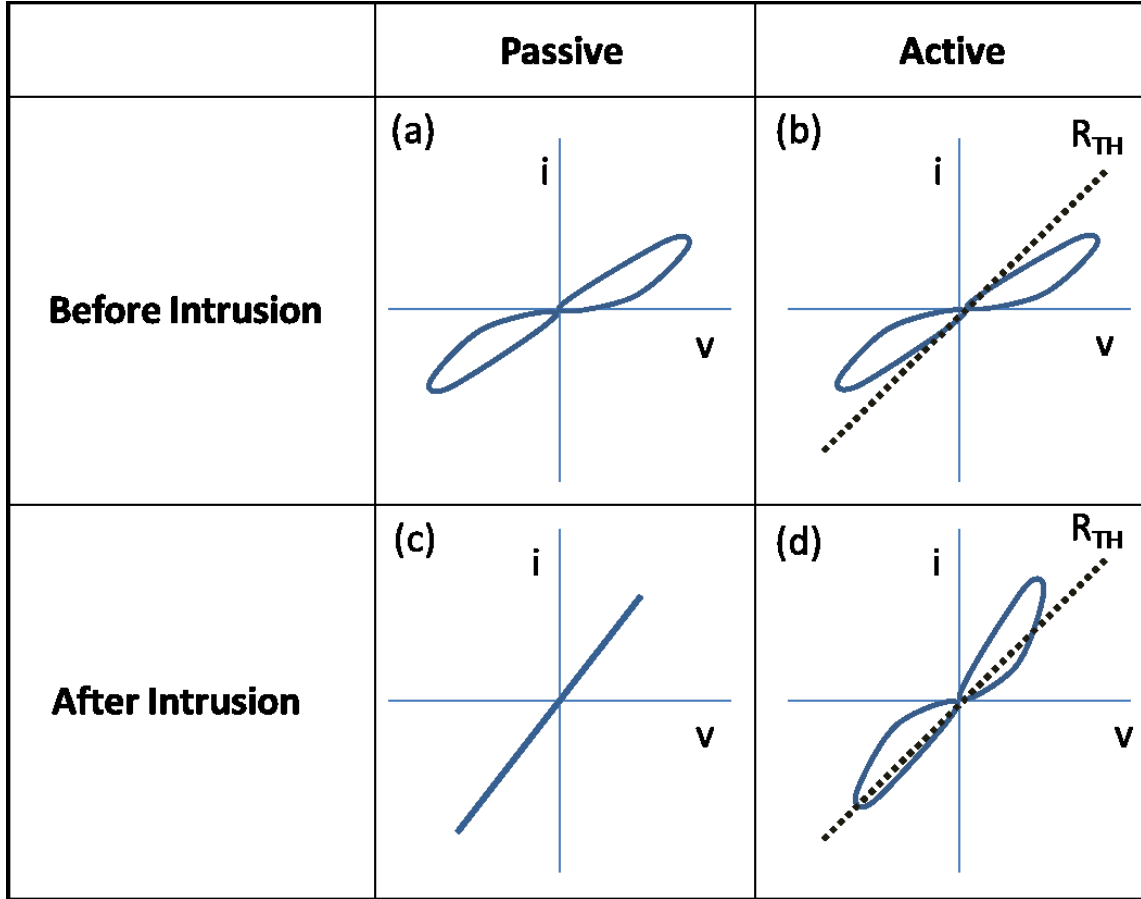
Figure 2: Examples of IV traces for active and passive monitoring before and after intrusion of a device.

The electrically tunable traits (by population and surface condition) of this device allow for potential with various electrical and mechanical ranges, further investigations will be discussed in the future works section into possible tunability for climate. The

jammed particle memristor surface condition provides tunable outputs by the controlling of the oxide thickness with force as well (shown in blue, Figure 3.)

Figure 3(a) below shows the granular application of a simple memristive system of two particles. The particles in the instance of this thesis were copper with a thin oxide layer on each. When the particles interact, the system of interest for this thesis becomes similar to Figure 3(b) and 3(c). This oxide layer essentially varies its resistance when different voltages and forces are applied. A more complete discussion of the workings of a memristor will follow in later sections. While the electrical properties have an effect on local resistivity, forces pressing the two particles together will be shown to have a significant effect aswell by the change in contact area. The 1-Dimensional array will show the simplification of interaction between the particles in higher dimensional devices.
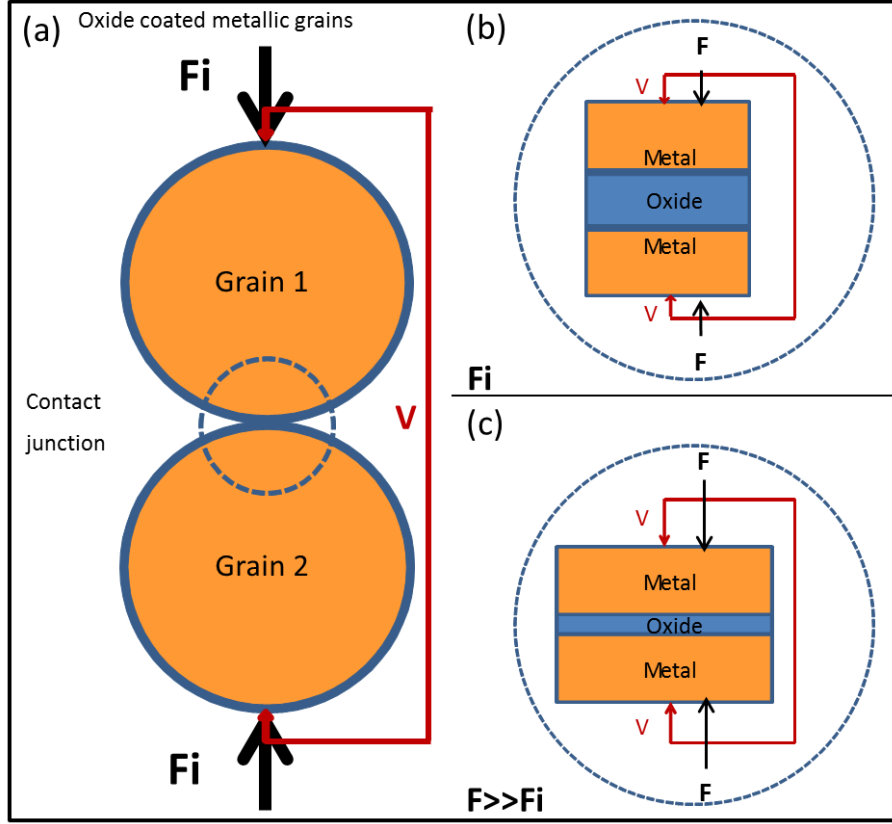
Figure 3: (a) Shows a two dimensional cross section of two copper sphere grains covered in thin oxide layer. Image (b) is at low load, in this loading state the contact area between the grains is small, and the oxide layer is thick. When a higher loading condition occurs, as is seen in image (c), the contact area increases and thickness decreases. Figure data from [17].

Applications extending to other fields are possible for traditional lithographic memristors, in addition to the proposed granular memristor system. One such application of traditional memristors is the replacement of transistors for the functioning as a memory device and also for computing purposes due to the memristors non-volatile characteristics as well as low power consumption and scalability. Other devices have been proposed to simulate neural behavior with memristors [33, 20]. A jammed granular memristor system could possibly be adapted to these purposes as well. The term jammed

9

is presented in the title as well as the bulk of the paper; this is used to express a simple static compressive force state of organized spheres.

Research Scope

To that end, this research project inquires: Can a copper granular Memristive system be characterized with respect to forces and voltages applied? Will the user be able to discern handling by setting threshold values of mechanical and electrical properties for specific devices?

The research shows the feasibility of this type of system protection sensor by proving the 1-D model, in the form of a single line of jammed copper granules (spheres). 2-D, and 3-D models will be left to future work and can be expected to be systems of planes and volumes of spheres respectively. The primary objective consists of a predictable system relating forces to current and resistance measurements through the contact areas between multiple oxidized copper spheres.

Overview

This thesis will continue to Chapter 2 where the interface behavior between spheres will be discussed in terms of contact mechanics along with an explanation of the behavior of a memristor device. These explanations for mechanical and electrical properties will be combined and depict how they apply to the jammed copper granular media. A research approach and procedure will then be introduced in Chapter 3 before finally including work that has been completed to the present time in Chapter 4 and 5.

II. Literature Review

To continue this thesis, the theory behind characterization of this sensor will be discussed further. The local workings of the proposed copper granular memristor will be considered in comparison to 'traditional' lithographically grown memristor theory. Previous works with nonlinear resistive elements in metal-insulator-metal (MIM) systems will be presented in Chapters 2 before the mechanism most likely present is proposed in Chapter 4 with results. As discussed in the previous chapter, the goal for this thesis is to create a predictable one dimensional jammed granular memristor system to lay the groundwork for future 2-Dimensional, and 3-Dimensional applications. Such higher dimension devices should provide more directional sensitivities as well as complexities to limit unobservable intrusion.

Branly Effect

A similar phenomenon of a granular device had been seen more than 120 years ago by Édouard Branly [13]. Branly found that if metal filings were placed between two electrodes, a high resistance state would be measured, the device essentially in an 'OFF' state [13]. Following a nearby electrical spark the high resistance state would suddenly become a low resistance state, turning the device 'ON'. This device was first known as a 'radio-conductor' by Branly in 1890, and later a 'coherer' by Lodge in 1893 [13]. The low resistance state would be observable for up to 24 hours [13]. The device could then be turned back 'OFF' by bumping the filings, thus resetting the system to a high resistance state. Branly's device, was tested up to 20m away from the spark source, this led the way for the 20th century [13]. Although Branly was able to create the device, as

an accomplished physicist and physician, he was not able to prove a definite mechanism of this sudden conductance [13].

Guglielmo Marconi, who is better known for his commercialization of radio communication by means of crystal detectors and success with radio communication followed Branly's discovery in this accomplishment [13]. Marconi accomplished a major feat of the time; Marconi passed a radio signal across the English Channel. This groundbreaking transmission: "Mr. Marconi sends to Mr. Branly his regards over the Channel through the wireless telegraph, this nice achievement being partly the result of Mr. Branly's remarkable work."[13]

A "ball coherer" was designed and built by Branly in 1899 using metal spheres with the same results as the metal filings; further research has been carried out more recently on the conduction of granular materials by E. Falcon [8]. Falcon looked further into spherical particles and packing behavior with pure copper, brass, bronze and stainless steel particles in 1 and 2 Dimensions. Hysteretic responses in current-voltage plots were to be seen at different contact conditions by varying compression forces, as is seen in Figure 4 [8]. Falcons' work in Figure 4 shows a significant shift in the 'ON' state of the device to lower resistance with increased force, in addition it should be noted, no surface preparation was mentioned for the stainless steel sphere array.
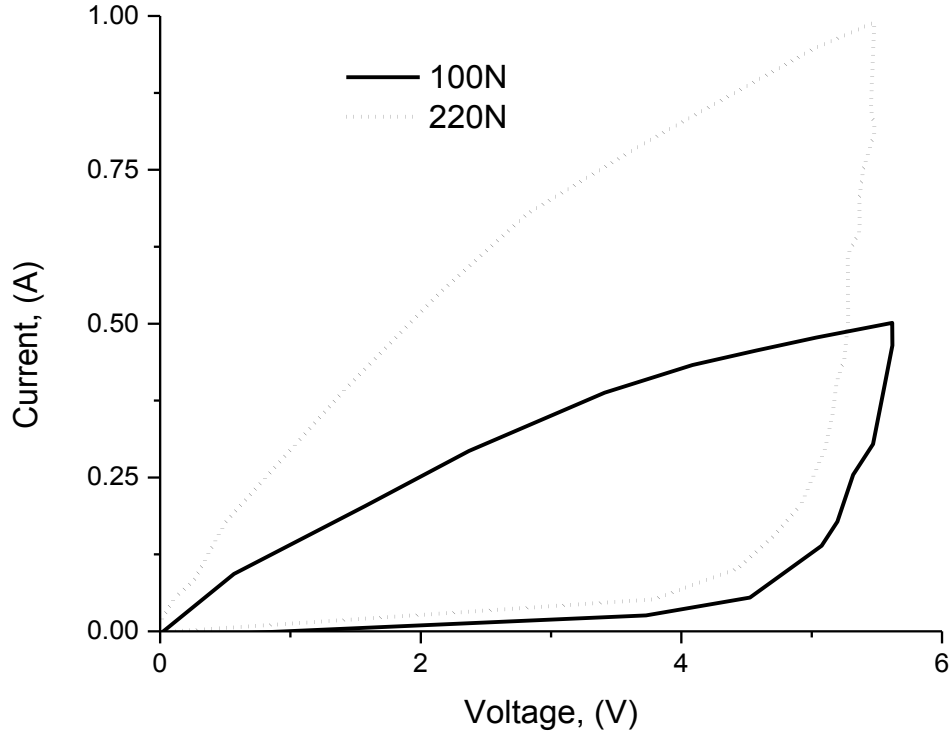
Figure 4: E. Falcons' hysteretic response to an IV trace with varied force in 8mm diameter stainless steel spheres. As force (contact area) increases, the hysteresis loop 'ON' state (top of loop) shifts to a lower resistance state. Figure data from [8].

Additionally, Falcon proposed micro welding phenomena mainly due to joule heating at the surface contacts [8]. The equation given for local contact temperature is as follows,

$$Tm = \sqrt{T_o^2 + \frac{V^2}{4LN_C^2}} \qquad (1)$$

13

Where *Tm* is the local temperature of the sphere contacts, *V* is the applied voltage, *L* is the Lorentz constant, and N_C is the number of contacts in the chain (number of spheres plus one) [8]. With this equation, Falcon claims that the local temperature is independent of materials properties and contact geometry [8].

The work proposed in this thesis is focused on the similarity in the electrical response of the granular array to compressive loading.

Sphere-Sphere Contact

To generate our own understanding of the contact conduction mechanisms, we look to Heinrich Hertz. Heinrich Hertz introduced his theory to the elastic behavior of two spherical materials in contact with one another in 1882 [15, 26]. Using Hertz model, others have modified the equations to take into consideration adhesive forces resulting in more accuracy in lower loading conditions [15]. For the purposes of this thesis we will be applying Hertz model due to the relatively unknown surface conditions. The most important relation for this thesis is the dependence of contact area between spheres on the applied force, *F* in Newton's between the spheres, equation 2 below shows the specifics of this relation [15].

$$Area\ of\ Contact = \pi \left(\frac{3FD}{4E^*}\right)^{\frac{2}{3}} \tag{2}$$

E^* is the effective elastic modulus between two spheres in contact in units of Pascal's, and *D* is the effective diameter between the spheres in meters.

$$E^* = \left(\frac{1-v_1^2}{E_1} + \frac{1-v_2^2}{E_2}\right)^{-1} \tag{3}$$

$$D = \left(\frac{1}{r_1} + \frac{1}{r_2}\right)^{-1} \tag{4}$$

Where the variables E_1, E_2, r_1, r_2, v_1, v_2 are taken as the respective elastic moduli, respective diameters and respective Poisson ratios of the two interfering spheres. As is seen in Figure 5 below, when a force is applied, the two spheres come into contact at a flat circular interface between.
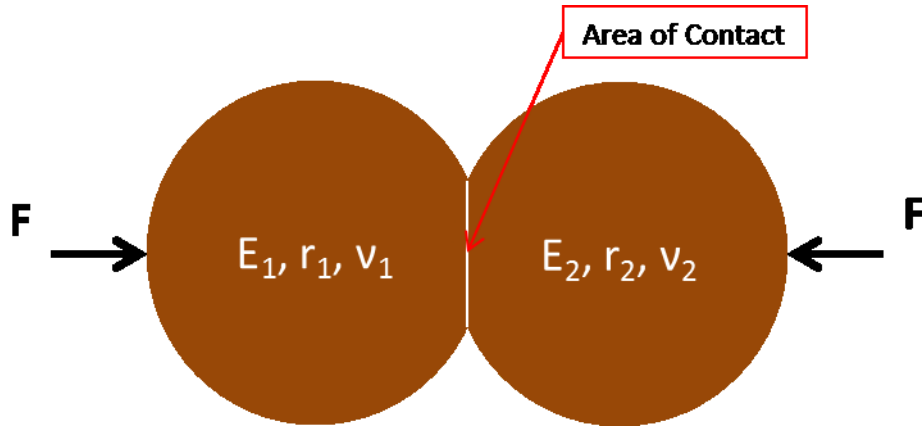
Figure 5: This figure shows two spherical materials in elastic contact to be described by Hertz equations. Each material has an Elastic modulus, a diameter, and a Poisson ratio associated with it.

To complete the necessity of these equations with respect to this thesis, we also know that classically, resistance decreases with increasing cross sectional area in a wire. The resistance, R (Ω) in a wire with cross sectional area A (sq. meters), length l (meters), and resistivity ρ (Ω-meters) is given by the following equation [27].

15

$$R = \frac{\rho l}{A} \qquad (5)$$

Combining equations 2 and 5 results in a relation for the resistance as a function

of force with constant resistivity in a sphere array. For the elastic region of contact

between two spherical particles and ignoring any mechanical interference of a thin oxide

layer, the resistance R should follow equation 6 with applied force, F.

$$R \propto F^{-\frac{2}{3}} \qquad (6)$$

Because the surface of the spheres can be relatively rough depending on

preparatory conditions such as extent of any etching and/or oxidizing, this relationship

will be shown to be the trend in some experimental data. Other mechanisms differing

from geometry change alone for resistance/conduction changes are observed. Since the

metal surfaces are bifurcated with an oxide layer, the resistance change is not expected to

follow this inverse relationship directly amongst voltage sweeps.   For the purposes of

this thesis, the elastic region was considered to be the main focus in comparing

memristive phenomena to geometry changes due to compressive force since some

approximate area is known.

In addition, Hertz contact mechanics between two solid spheres can be extended

to provide a critical loading condition in which the elastic region of compression is no

more. For this, Johnson looks to the Von Mises criterion, who defines the maximum

pressure $p_0 = 1.6 * Y$, where Y is the compressive yield strength of the material in units of

Pascal's [15]. The load to initiate yield at that pressure is given as F_Y in units of Newton's in equation 7 below [15].

$$F_Y = \frac{\pi^3 D^2}{6E^*} {p_0}^3 \tag{7}$$

Force Measure Theory

To have a better idea of whether compression is in elastic or inelastic regime of compression, an additional factor that will have to be considered is a simple cantilever in bending, in order to approximate compressive force across the granular array. The cantilever application will be further discussed in Chapter 3. According to elastic solutions to a simple cantilever with measureable deflection, the load at the tip of the beam is calculated using equation 8 [26].

$$-\frac{3EI\delta_{max}}{l^3} = F_{applied} \tag{8}$$

Where E is the Elastic Modulus of the beam in Pascal's, δ_{max} is the deflection of the beam in meters, l is the length of the beam in meters, and I is the second moment of inertia in meters[4]; given by equation 9.

$$I = \frac{\pi d^4}{64} \tag{9}$$

Where d in equation 9 is the diameter of the cylindrical beam in meters. Figure 6 below shows the appropriate variables to apply to equation 8. Since the beam was essentially fixed, the force on the end of the beam is equal to the equal and opposite force on the opposing end.
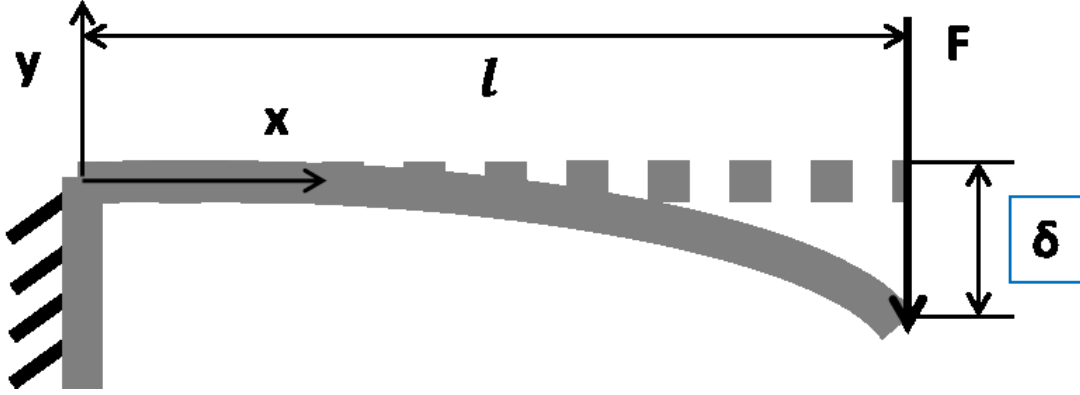
Figure 6: The figure depicts a simply loaded cantilever beam in bending. Where E is the Elastic Modulus of the beam, δ_{max} is the deflection of the beam, l is the length of the beam with diameter d.

Memristor / Metal-Insulator-Metal Interface

A memristor was first regarded to be the fourth fundamental electrical element in 1971 by Leon Chua, to compliment the resistor, inductor, and capacitor [16]. Chua made the argument for the memory-resistor due to symmetry as there was no basic circuit relation of magnetic flux to charge in a system [16].

Memristor theory in short suggests a change in conductivity between electrode connections to the device, usually through an oxide with respect to charge. This relation makes for a nonlinear voltage-current relation by the relation of magnetic flux and charge in the system [7].

$$M(q) = \frac{d\varphi}{dq} \tag{10}$$

Where $d\varphi$ is the change in magnetic flux, and dq is the change in charge. Although the relation was theorized by in the 1970's, an acceptable device with this

memristive behavior was not produced until 2008 by Strukov et al. [7]. The behavior of interest for the purposes of this thesis is specifically the ability of current to flow, or resistance switching of the device under applied compression, as the contact area changes. Possible mechanisms for the specific granular copper system presented in this thesis will be discussed later in this chapter.

A qualitative understanding of a traditional memristor increases the understanding of the granular system proposed. The memristor by Strukov et al. consisted of two platinum electrodes bifurcated by a titanium oxide (TiO_2) and a region of oxygen deficient titanium oxide. Once a potential is applied in one direction the TiO_2 is essentially doped by platinum ions decreasing resistance (Figure 7(b)) if a reverse potential is then applied, the platinum dopant is replaced by vacancies, thus increasing resistance (Figure 7(c)). Figure 7 below shows a representation of a memristor, in the conductive/resistive region between the electrodes. As the conductive platinum ions (for Strukovs' case) move with width 'w', filling oxygen vacancies, resistance drops and just the opposite is seen when reverse bias is applied [6]. A representative example of the IV trace that would result can be found in Figure 2(a) in Chapter 1.
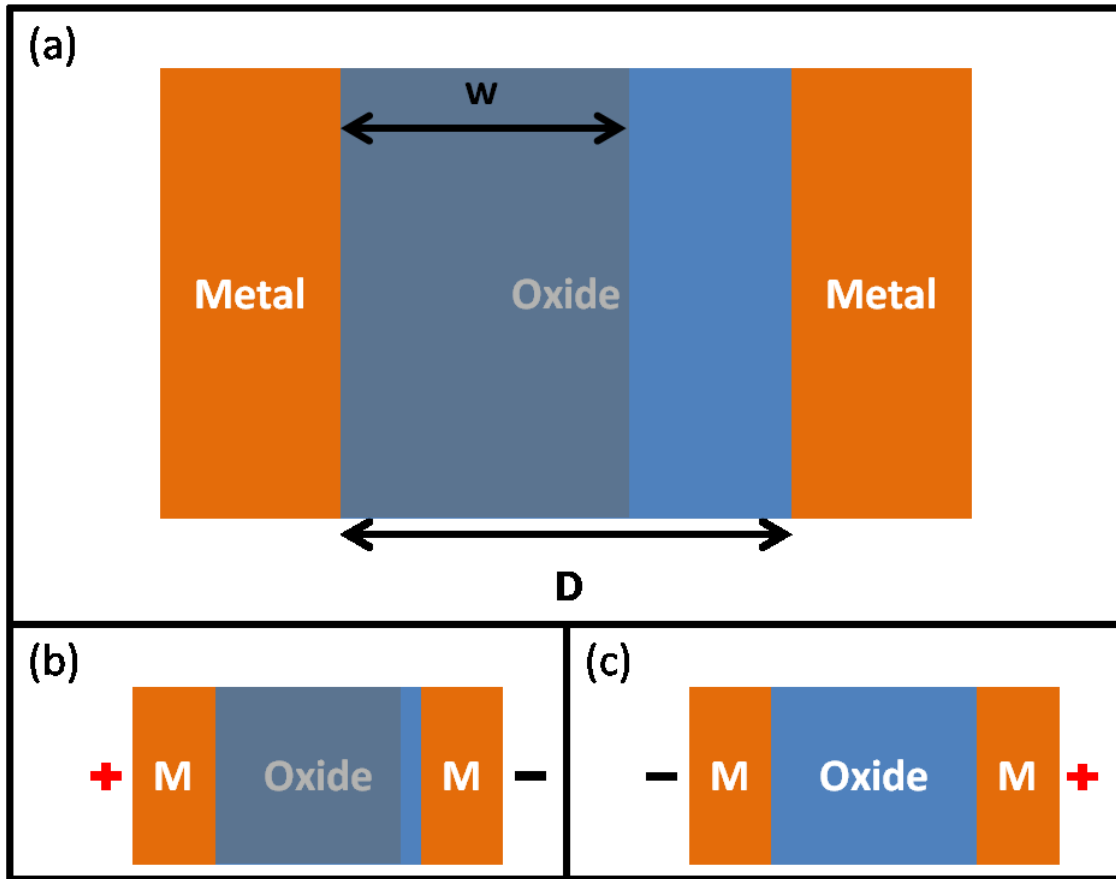
Figure 7: The resistive/conductive region shows the movement of the ON/OFF regions within an oxide. The ON/OFF states are produced by the movement of Pt ions (for Strukovs' case) in and out of the TiO_2. Figure data from Strukov [7].

Potential applications vary across many fields of study for memristors. The main being synonymous to the name memristor, memory applications are expected to outperform current memory hardware by scalability and power consumption.

Unfortunately Strukov's model only predicts a single dimensional memristor, in the case of a granular array memristor, with increased force; we have seen with Hertz equations an increase in contact area. Gale et al. looked into this phenomenon on planar memristors and saw a shift in the hysteresis loop to a lower resistance state with larger

electrode contact area [9]. Gale et al. showed experimental data with various electrode

sizes across a TiO$_2$ memristor. Using electrode widths from 1mm to 5mm long the

increased contact area showed significant difference in memristive characterization. As

the area increases the device hysteresis shifts into a lower resistance state for both 'ON'

and 'OFF' states [9]. For the purposes of a jammed granular array memristor, the subject

of this thesis, the contact area increases with compressive force and was expected to

behave similarly to Gale et al.

Gale observed a drop in resistance with increased contact area; this can be seen in

Figure 8 as the 'OFF' resistance change with increasing electrode contact area.
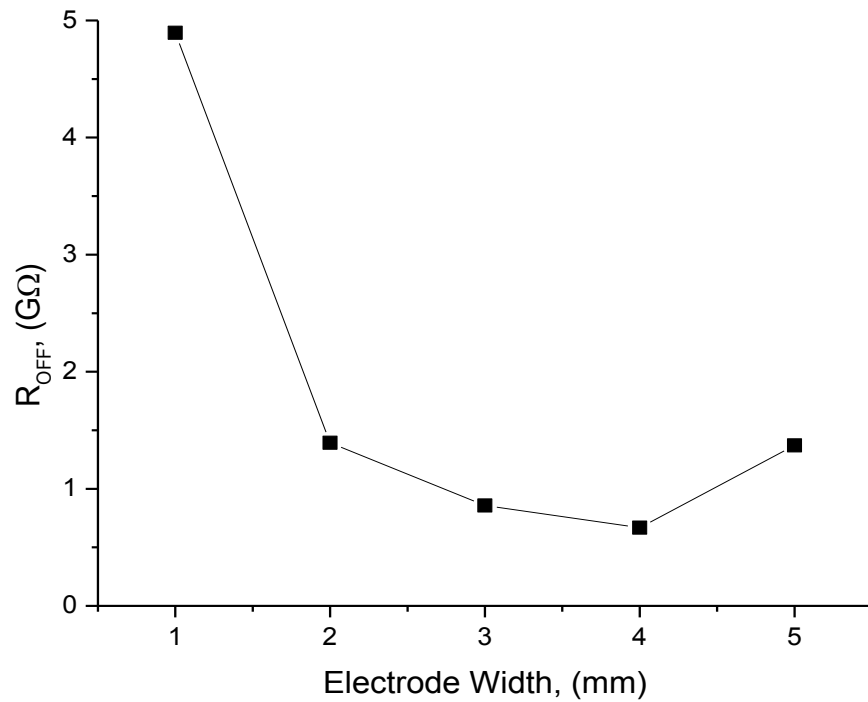
Figure 8: Figure data from Gale [9]. R$_{OFF}$, which is the lower portion of the hysteresis
loop (the high resistance state) is plotted against electrode contact size. As the contact
area increases, the 'OFF' resistance state decreases.

This thesis will look into the application to a system protection devices with this area change in mind within a copper-copper oxide granular system.

Nonlinear Charge Transport in an Oxide

Various charge transport phenomena in amorphous oxide films have been proposed by Dearnaley, Stoneham, and Morgan in their paper, *Electrical phenomena in amorphous oxide films* [11]. For this thesis, there is the possibility of an amorphous oxide due to the lack of periodicity of the copper substrate, although this is not certain, it is seen as a reasonable starting point. Dearnaley et al. have proposed that a phenomena previously attributed to an unspecific breakdown was due to 'pinholes' in the oxide which allowed for charge to travel through [11]. This conduction (typically electrons or holes due to their generally higher mobility), was found to be something much more than an anomaly [11]. Dearnaley et al. proposed the formation of a conductive channel. Within this forming process few characteristics were observed; the first of which a "profound and irreversible change" in the conductance, with a switching/memory behavior [11]. Various memristive systems show different charge transport domination, whether it be electron, hole or ion movement through the dielectric. Traditionally, electrons and holes are most mobile followed by ions. The equations in Table 2 were discussed by Dearnaley et al., and will be presented in detail [11].

With small enough oxide thickness, less than 5nm, it has been postulated by Dearnaley that the traditional understanding of electron tunneling is the dominant charge transport mechanism [11]. When the dielectric thickness is increased to a value greater than 5nm, the nonlinear behavior is thought to be either one or a combination of other

transport mechanisms, a summary can be found in Table 2. The mechanism or mechanisms responsible for the nonlinear current change in a sufficiently thick metal-insulator-metal system are yet to be fully understood. For the purposes of this paper, the electronic reactions, the physical deformation of the oxide and the metal must be taken into consideration when looking at stressed states of the memristive sphere contact.

The best fit for the single dimension copper sphere array will be discussed along with reasoning for such a decision in Chapters 4 and 5.

Since the size of the inter-sphere contacts is sufficiently small, along with the oxide thicknesses of the experimental setup being assumed to be small, (explained in Chapter 3) the current densities J and electric field E are expected to be rather large and rather small respectively for low loading conditions. As loading increases, the inverse is seen, in that the oxide decreases thickness slightly thus increasing E, and the contact area increases decreasing J. For the carrier transport mechanisms introduced in Table 2, electric field against a logarithmic current density were used to determine the best conduction mechanism of the most likely candidates [1]. A continued discussion with copper sphere results can be found in Chapter 4.

Schottky barrier theory models conduction through a semiconductor by evaluating carrier diffusion and drift across the depletion region near the interface in a metal-semiconductor system [29]. This assumes that space-charge region is sufficiently large thus making the diffusion constant and mobility relevant [27]. Schottky, also known as thermionic emission is an acknowledged model for conductance through insulators.

Poole-Frenkel emission, much like thermionic emission, Poole-Frenkel emission results in the field-lowering of the barrier height [1]. The main difference is that Poole-Frenkel assumes a point defect surrounded by a Coulombic Potential and a position in the crystal lattice in which donor type behavior occurs [11]. The Poole-Frenkel relationship presented in this paper is specific to only one dimension carrier transport, Jonscher proposed a three dimensional modification, which can be found in the references [1]. This modification states that the "carrier emitted from a trap site from the field once free, will be re-trapped by the nearest next site" [1]. "This distance traveled before re-trapping is independent of applied field and directly proportional to probability of emission" [23].

Hopping conduction, unlike Schottky and Poole-Frenkel has four characteristic features to obtain before any conclusions can be made. From A.K. Jonschers' paper on electronic properties of amorphous dielectric films, the typical features of hopping can be found by the following table [1].

Table 1: Jonschers' characteristics of hopping conduction [1]

(a) Linear dependence of current on voltage
(b) Low activation energy
(c) Increase of AC conductivity with frequency
(d) A slight decrease ability to polarize with frequency"

No temperature dependent measurements were carried out on the jammed granular array; therefore we cannot discard contribution due to hopping alone

Space Charge Limited current, also known as the Mott-Gurney relationship is devised from dopant and free carrier concentrations [11]. This behavior is modeled assuming carrier and doping concentrations are in equilibrium at the semiconductor-metal interface [29]. When a bias is applied the movement of electrons or holes breaks this equilibrium and a space charge effect is said to be present [11]. "This iterative current-voltage relationship", consists of the field dominating the current, while simultaneously the current establishes the field [29].

Similar to diffusion, Ionic Conduction follows an exponential law, dependent with temperature [29]. When the material is in an amorphous state, such that the metal is for this thesis, the average bond energy is much higher due to the strain in the lattice. These higher energy states result in less energy required to break bonds, thus allowing the larger ions to migrate with less energy when current is applied. Although this seems to be applicable to the thesis at hand, ionic mobility's are generally a few orders of magnitude lower than that of electrons or holes [11].

An investigation into the majority carriers will be discussed in the future works section of this paper with impedance spectroscopy. Tunneling was not considered for this thesis due to the oxide thickness approximation being greater than 5nm, to which Dearnaley stated tunneling is no longer significant [11]. Table 2 below summarizes the previously described conduction mechanisms.

Table 2: Charge Transport mechanisms. J is the current density, Δ_B is barrier height, E is applied field, A is Richardson constant, Δ_H and Δ_I are activation energies, μ is electron mobility, d is thickness, G is the conductivity, T is temperature, k is Boltzmann constant, B is a best fit constant. Equations in table below discussed in [11].

(a)	**Schottky**	$J_S = AT^2 \exp - \left(\dfrac{\Delta_B}{kT} - \dfrac{\alpha\sqrt{E}}{kT} \right)$
(b)	**Poole-Frenkel**	$J_{PF} = BE \exp - \left(\dfrac{\Delta_B}{kT} - \dfrac{2\alpha\sqrt{E}}{kT} \right)$
(c)	**Hopping**	$J_H = J_0 \exp - \left(\dfrac{\Delta_H}{kT} \right)$
(d)	**Space Charge Limited**	$J_{SCL} = e\mu \dfrac{E^2}{d}$
(e)	**Ionic Conduction**	$J_I = \dfrac{GE}{T} \exp - \left(\dfrac{\Delta_I}{kT} \right)$

Pressure/Area Dependent Properties

For the purposes of the system of constant volume, when compressing in a direction, the bonds parallel to the compression forces will become shorter, forcing transverse bonds to elongate by Poissons' effect [31]. This should allow for higher ionic mobility in the axial direction of compression for an elastic region of compression in a periodic lattice structure. Poissons' relation can be found as v, which relates strain in orthogonal directions, an example can be seen in the equation below, where ε_x is strain with respect to the x axis, similarly, ε_y for y axis, and ε_z for z axis.

$$v = -\frac{\varepsilon_x}{\varepsilon_z} = -\frac{\varepsilon_y}{\varepsilon_z} \tag{11}$$

Figure 9 below shows a representation of an applied compressive strain, and the resulting tensions in the orthogonal directions on an FCC unit cell. FCC is the lattice parameter for polycrystalline copper and an ideal case, although we will see in Chapter 3 the copper spheres are amorphous, Poisson's effect should still apply to some extent. In the amorphous system, compressive strain should result in transverse tension. This type of atomic movement can also be applied to the oxide between spheres as compression ensues. The atomic movement would be beneficial for carrier transport within the dielectric material due to the weakening of bonds in the direction of applied field/force (x direction).
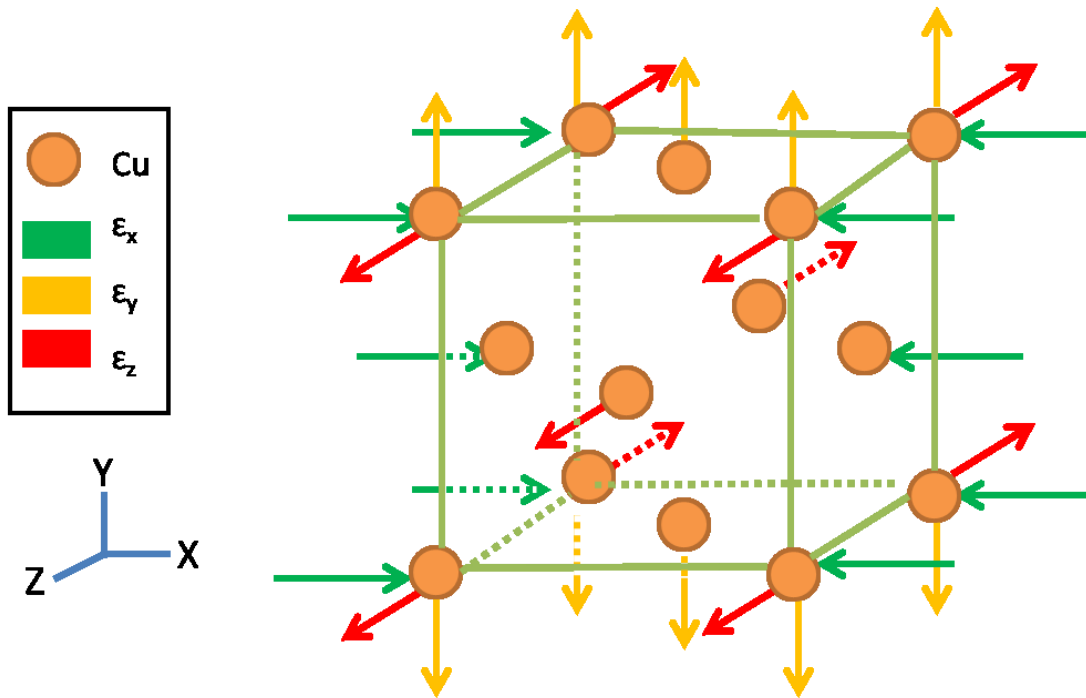

Figure 9: This figure shows a typical FCC unit cell under an applied compression load in the x direction. Assuming relatively unrestricted movement in the y and z directions, the applied compression will result in a tension in the y and z axes. This is an example of Poisson effect. Figure data from [31].

Y. Kim et al. saw compressive-electrical relations in NiO in their paper

Mechanical Control of Electroresistive Switching [34]. Kim et al. were able to

demonstrate forcing a device to high resistance state with an applied pressure (OFF state),

and back to a low resistance (ON state) with an applied negative voltage [34]. From this

observation along with the information learned from the paper by Dearnaley et al. this

could suggest some type of unidirectional filament growth with the application of a

negative bias, allowing for conduction [11]. When the pressure is applied, the filament is

possibly fractured ceasing conduction, thus resuming the high resistance (OFF) state.

Materials Properties

Commercial off the shelf copper spheres were used in this thesis, obtained from

itiball.com. Copper was chosen for its well defined mechanical and electrical properties,

it was also seen by Castle to be memristive under certain thermal oxidation conditions

[4]. Basic X-Ray techniques such as X-Ray Diffraction (XRD) and X-Ray Photoelectron

Spectroscopy (XPS) were applied to determine relative bulk and surface characteristics

respectively. As a result of the XRD data, nano-indentation was employed to determine

mechanical properties of the copper spheres.

X-Ray Diffraction

X-Ray diffraction consists normally of a metal target, emitting characteristic X-

Rays at wavelength, λ. These characteristic X-Rays are aimed at a sample at an angle θ

and reflect off into a detector as is seen in Figure 10. Using Bragg's law, the

predominant planes in the specimen under analysis can be determined from the reflected data. Bragg's law is commonly written as the following equation.

$$n\lambda = 2d_{hkl}Sin(\theta) \tag{12}$$

Where d_{hkl} is the inter-planar spacing, seen in Figure 10, and n is the order of reflection which is an integer [31]. Meyers showed significant changes in mechanical properties dependent on crystallinity of copper samples [18]. Specifically, Meyers showed an increase in yield strength with decreasing grain size [18]. When grain size is sufficiently small, the sample is essentially an amorphous structure. Hertz contact mechanics discussed earlier are dependent on this yield strength for the onset of inelastic compression of granule spheres; similarly the elastic modulus plays a role in this deformation as well. XRD provided us more information on the crystallinity or lack thereof of the copper spheres, leading to nano-indentation measurements to acquire more mechanical property information.
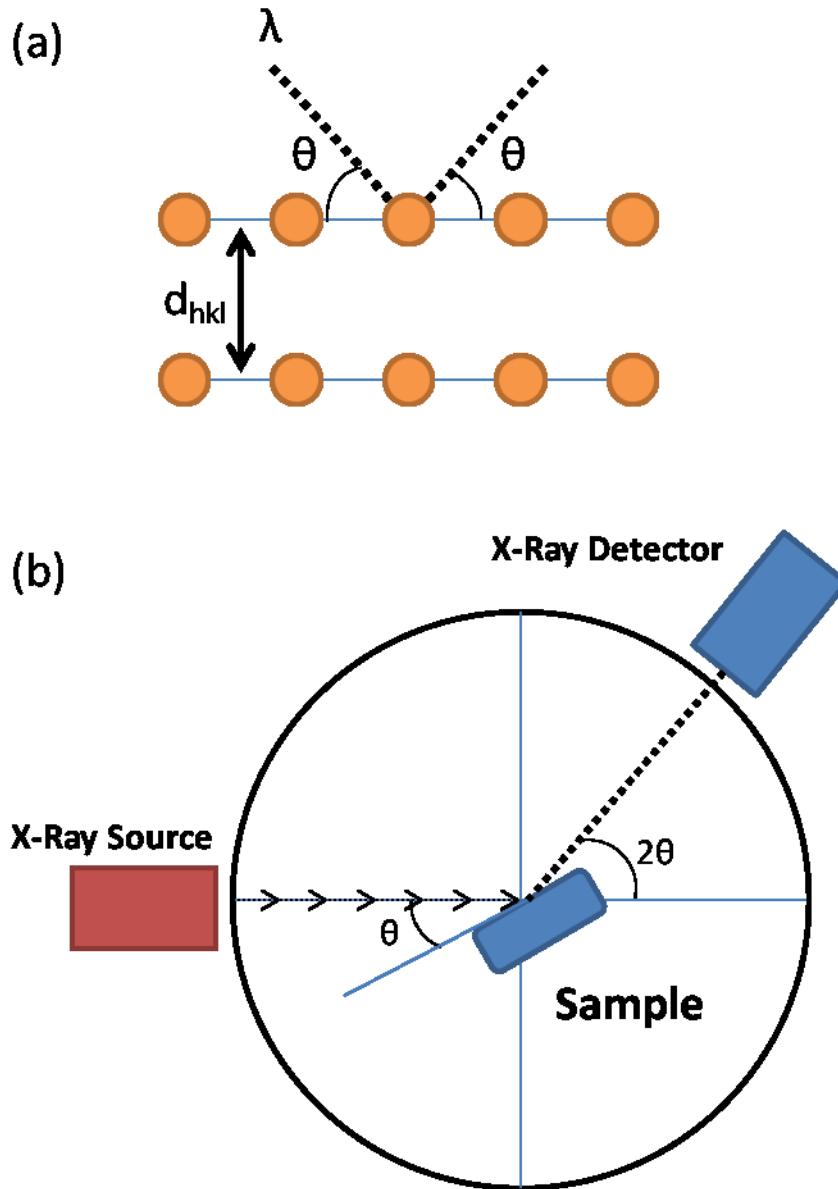
Figure 10: Image (a) shows incident X-Rays of wavelength λ hitting an atomic plane at an angle θ, with inter-atomic spacing d_{hkl}. The measured diffracted X-Ray is then plotted in counts versus two times the angle measured. Further processing of data using Bragg's equation will produce the planes in the sample in hkl coordinates. Image (b) is a representation of an experimental setup for XRD. Figure data from [36].

In the particular case in which the sample is not polycrystalline, in that d_{hkl} does not repeat consistently throughout any part of the sample, the sample is then said to be

amorphous. Figure 11 shows representative X-Ray diffraction spectra of counts versus

2θ in an amorphous and crystalline metal. The crystalline metal shows distinct peaks that

can be related to specific crystalline planes in the lattice, the amorphous spectrum shows

little resolution in comparison.
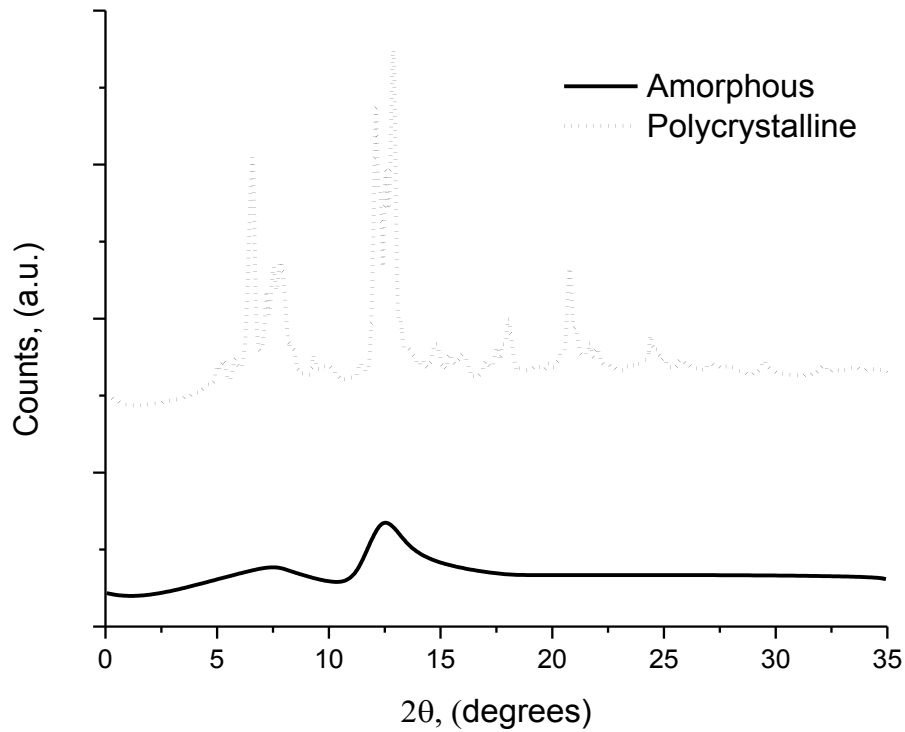
Figure 11: A representative crystalline versus amorphous X-Ray diffraction pattern for a
metal. There is a significant drop in peak count, intensity, and resolution when
comparing an amorphous sample with a polycrystalline sample. Figure data from [36].

Nano-indentation

Nano-indentation uses a sharp tip of known geometry to deform the material all

while measuring displacement and resulting resistant force. Figure 12 shows a typical

nano-indentation curve, where the y-axis is the load resisting indentation (in units

31

Newton's), and the x-axis is the displacement into the surface (in units of meters). We

used the ASTM standard E2546-07 to analyze data [3]. The plot begins from the origin

at zero for both values and follows an increase to a predetermined depth or force for our

measurements. Once at that threshold, the machine holds for an amount of time and

begins to unload, this unloading has been determined to be the stiffness of the material

[3]. Knowing the stiffness of the material there is a method to find the resulting elastic

modulus of the indented material is explained below.

Figure 12: This figure shows a representative load-displacement curve for a typical nano-indenter. Starting from zero, the indenter tip is pressed into the surface to a predetermined depth or lo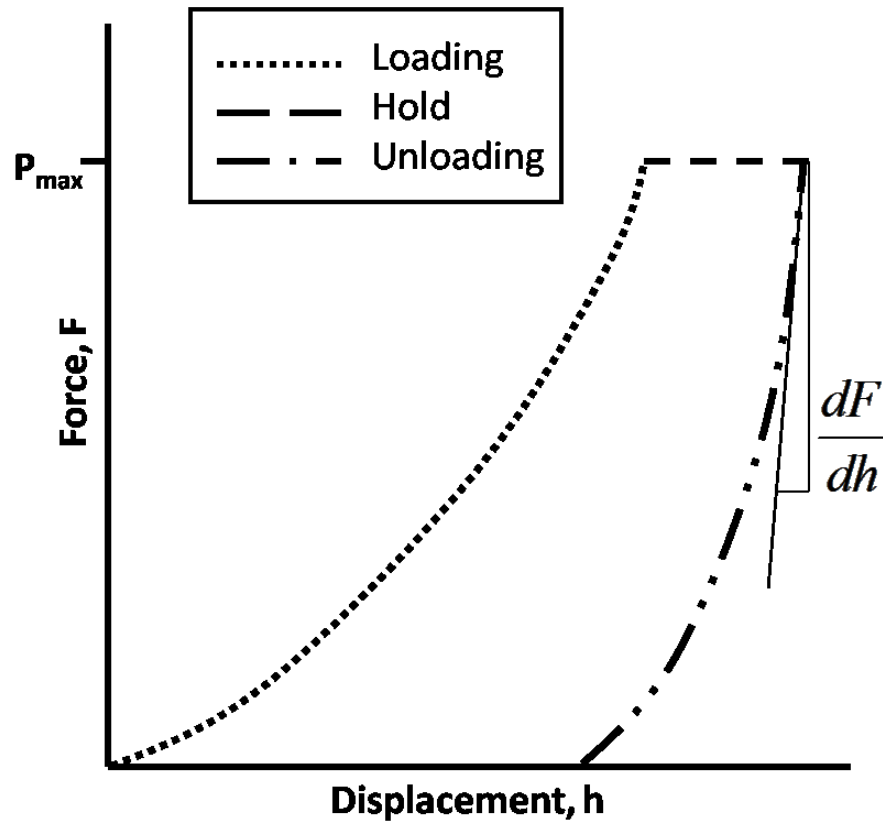ad threshold before it is unloaded. The unloading curve provides usable stiffness data for elastic modulus determination. The maximum load provides approximate yield strength in compression. Figure data from [3].

The process of modulus determination starts with the unloading curve of a typical indentation curve from Figure 12 [3]. The first 50-90% of the unloading data will be functionally related to the power law with the relationship [3].

$$F = B(h - h_f)^m \qquad (14)$$

Where the terms B, m, and h_f are best fit constants in the power law functional relationship. Once the constants are fit to the unloading curve, the stiffness, S, can be determined using the following relation

$$S = Bm(h_{max} - h_f)^{1-m} \qquad (15)$$

The stiffness value, S is in units of force per unit length, where h_{max} is the maximum penetration depth of the indenter. This stiffness can now be applied to the reduced equation for indentation modulus given by equation 16.

$$E_r = \frac{S}{2}\sqrt{\frac{\pi}{A}} \qquad (16)$$

Where A is the contact area, which is a function of depth and can be geometrically found as equation 17.

$$A = 25.4h^2 \qquad (17)$$

Taking h to be the depth of the nano-indenter for the first 50% of the unloading

curve relationship, from the reduced modulus E_r, the modulus of indented material can be

found using the following equation.

$$E_{IT} = \frac{(1-v_s^2)}{\left[\frac{1}{E_r} - \frac{(1-v_i^2)}{E_i}\right]} \tag{18}$$

E_{IT} is given as the indentation modulus, or the modulus of the material being

indented, E_i is the modulus of the indenter typically assumed to be 1140GPa for diamond

tips [3]. v_i is the Poisson ratio of the indenter, the typical value is 0.07 for diamond, and

v_s is given as the Poisson ratio of the material being indented. Since little information is

known about the material being indented, an approximation is given for $v_s = .25$ is

accepted with ±5% uncertainty [3].

Additionally, the compressive yield strength of the material, i.e. the amount of

stress at which first yield occurs is found from the nano-indentation data as the following

equation [15].

$$Y = \frac{H}{3} \tag{19}$$

Where Y is the approximate yield strength, and H is the hardness of the material in

Newton's per meter. And H is calculated as equation (20) [15].

$$H = \frac{F_{max}}{A_{max}} \tag{20}$$

Where F_{max}, and A_{max} are both values taken at the highest displacement into the material, see Figure 12, at the hold section.

X-Ray Photoelectron Spectroscopy

Simple X-Ray Photoelectron Spectroscopy (XPS) techniques were utilized to determine surface characteristics of the 'as received' spheres meaning no post purchase etch or oxidation was present. These surface conditions will provide pertinent information as to the mechanical and more so electrical properties within the proposed compression array. XPS only penetrates the first few layers of atoms, for this reason an Argon Ion sputter depth profile was employed in conjunction to XPS on the copper spheres [36]. This sputter depth profile takes a surface survey, ablates the measured surface with ions of Argon before measuring the new surface layer. Figure 13 shows a simple XPS setup without showing an Argon sputter setup.
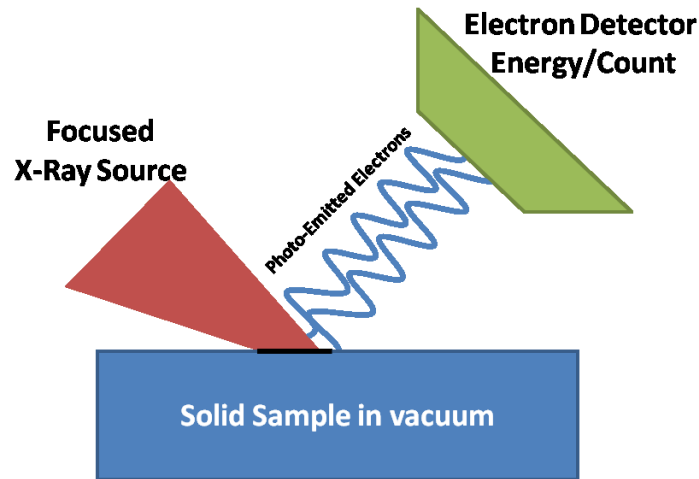

Figure 13: This figure depicts an ideal X-Ray photoelectron spectroscopy (XPS) experiment. A beam of X-Rays is focused onto a sample; the photo-emitted electrons escape. Knowing the X-Ray energy, the reflected electrons are collected by an analyzer and processed to determine binding energy [36]. Figure data from [36].

The XPS system emits X-Rays, at a known energy E_{photon} and subtracts from this energy the sum of the energy of the electrons removed from the sample, $E_{kinetic}$ and the work function, ϕ of the spectrometer. The equation for binding energy is shown as equation 13 [36].

$$E_{Binding} = E_{photon} - (E_{kinetic} - \phi) \tag{13}$$

XPS measurements are generally utilized for planar samples, and there exist some methods for determination of surface layer thickness for such samples. Due to the samples for these measurements being spheres, no reasonable assumptions can be made for oxide thickness due to geometry and scattering of the X-Rays and resultant removed electrons from the hemispherical surface. The detector is not as efficient on a hemispherical surface as it would have been on a flat surface.

Overview

To continue this thesis, Chapter 3 will discuss the analysis and characterization of the granular media chosen for this application. This includes the previously mentioned XRD, XPS, and nano-indentation results as well as some Scanning Electron Microscope (SEM) images. With this information we can continue on to introduce the testing apparatus before finally reaching the results in Chapter 4 and conclusions in Chapter 5.

III. Methodology

Chapter 3 of this thesis will continue on to an application of the information discussed for the various characterization methods in Chapter 2. In addition to the nano-indentation and various X-Ray and techniques a simple dimensional analysis using an SEM will be discussed as well as the experimental apparatus to relate simultaneous mechanical and electrical properties of the jammed granular memristive array.

SEM and Dimensional Analysis of Copper Spheres

Commercial off the shelf (COTS) materials are easily accessible, and seen as a great advantage in prototyping instances such as this. As mentioned in Chapters 1 and 2, copper spheres were purchased from a company called *Industrial Tectonics Inc. (itiball.com)* with the statement of 99.95% minimum copper; stating the residual is most likely silver [12]. Their stated sizes and tolerances can be found in the table below, and are said to be made of oxygen free high conductivity copper [12].

Table 3: The tolerances for the copper spheres purchased COTS for the purposes of testing memristive responses to jammed granular copper systems. Data from [12].

Property	Tolerance Value
Diameter	±5.08 μm
Sphericity	±10.16 μm
Finish	0.127 μm

These values seemed similar to actual values measured using a Zeiss SEM and processed with Zeiss AxioVision software. The average diameter of the micro-spheres was needed to ensure appropriate conditions for single dimension constraints for the case

of this thesis, the spheres would be aligned in a capillary tube with slightly larger inner diameter than the sphere diameter. Figure 14 below shows a random group of eleven 'as received' spheres, the average diameter was determined to be approximately 711μm, with a standard deviation of 10.46μm which is slightly larger than the tolerance from the manufacturer, but could be subject to aberrations of the focal length in the SEM imaging a hemispherical surface. This standard deviation is relatively small as compared with sphere diameter; although this is double the published tolerances it is very well possible the population for this representative sample was too small. This difference with the published tolerance in diameter by 'itiball' was not seen any danger to our experimental results.
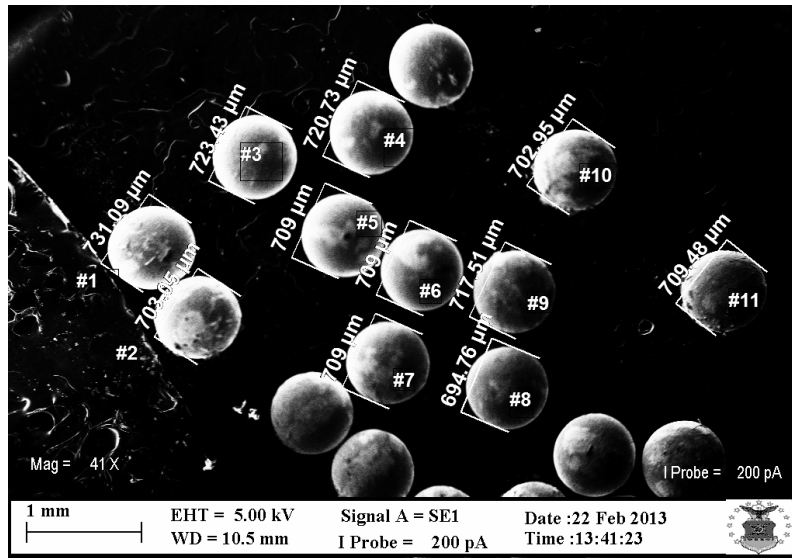

Figure 14: The SEM image taken resulted in an average sphere diameter of 711μm, and a standard deviation for the 11 random spheres of 10.46μm. This standard deviation is similar to the published values by the company providing the COTS spheres. SEM image courtesy of Dr. Daniel Felker AFIT/ENV.

Another point of interest is the sphericity; Figure 15 shows a representative example to provide an understanding for the sphericity. Across the three measurements taken the largest difference in diameter is 4μm. This value again was not seen as an immediate threat to experimental procedures.
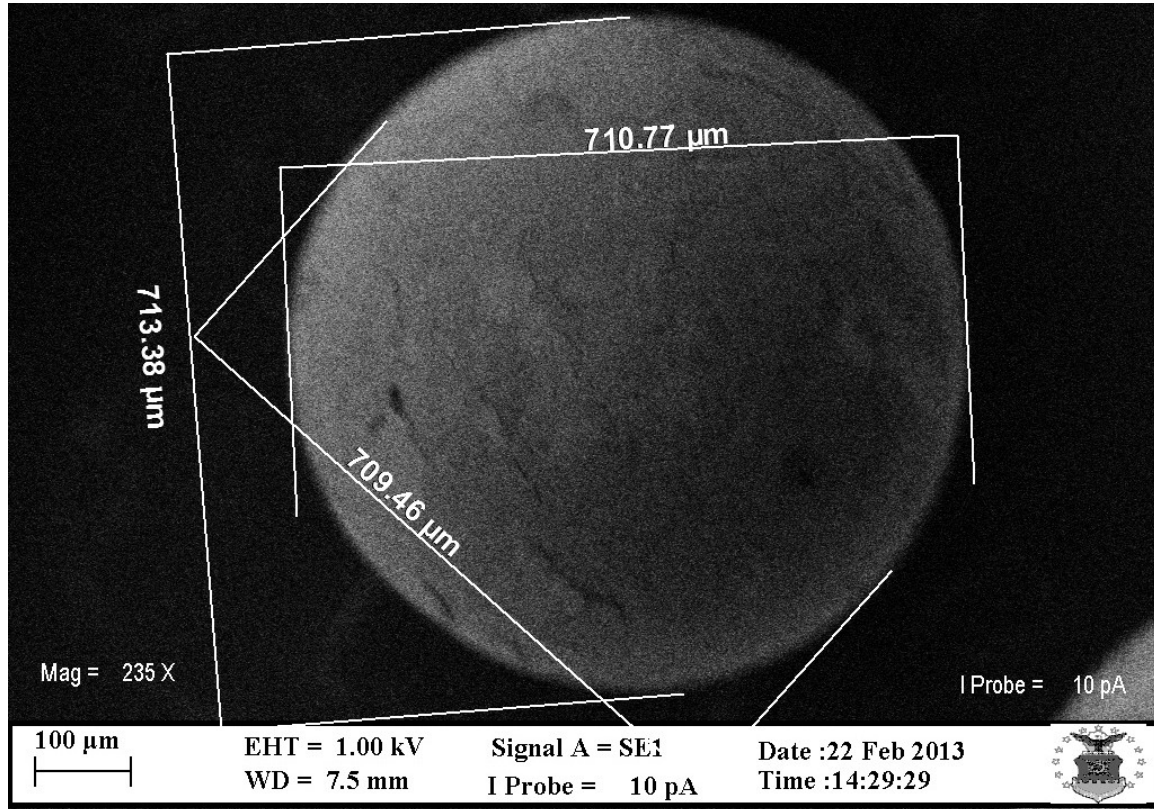
Figure 15: This figure shows a copper sphere with multiple diameters measured. This small change in the diameter at the different angles suggests there is much uniformity to sphere diameter. It can also be stated that across multiple different view angles on many spheres, no obviously oblong spheres were present. SEM image courtesy of Dr. Daniel Felker AFIT/ENV.

To test nonlinear resistance responses to compression and varied voltages in a single dimensional array, the spheres must be constrained to a single dimension, a

borosilicate capillary tube was selected due to it having 1E15 Ω-cm resistivity, making it highly insulating so as to not interfere with electrical measurements [31]. The tube used had a listed inner diameter and tolerance of 762μm and ±76.2μm respectively. For the worst case of misalignment of spheres, the maximum inner diameter is 838μm, 127μm larger than the average sphere. This packing will have an effect on force measurements and will be addressed later in this chapter.

X-Ray Diffraction

Figure 16 shows the experimental X-Ray Diffraction data for a group of randomly selected spheres 'as received'. The data points to the fact that the copper spheres are non-crystalline [35]. This leads to speculation of the creation of the spheres, (as the actual process from the supplier is proprietary) the spheres were likely quenched rapidly before the atoms had time to crystallize. Most likely liquid copper was poured in distinct quantities into a cool chamber, as the droplets fell to the liquid, the liquid copper naturally formed the shape of a sphere so as to reduce it surface area and in turn its surface energy [5]. Figure 16 shows indistinct XRD spectra for the copper spheres. The initial intensity at low 2θ values is due to the geometry of the machine. At approximately 45 degrees a slight trace of crystalline copper may be present, (see Figure 17) longer iterations time could improve resolution of this spectra.
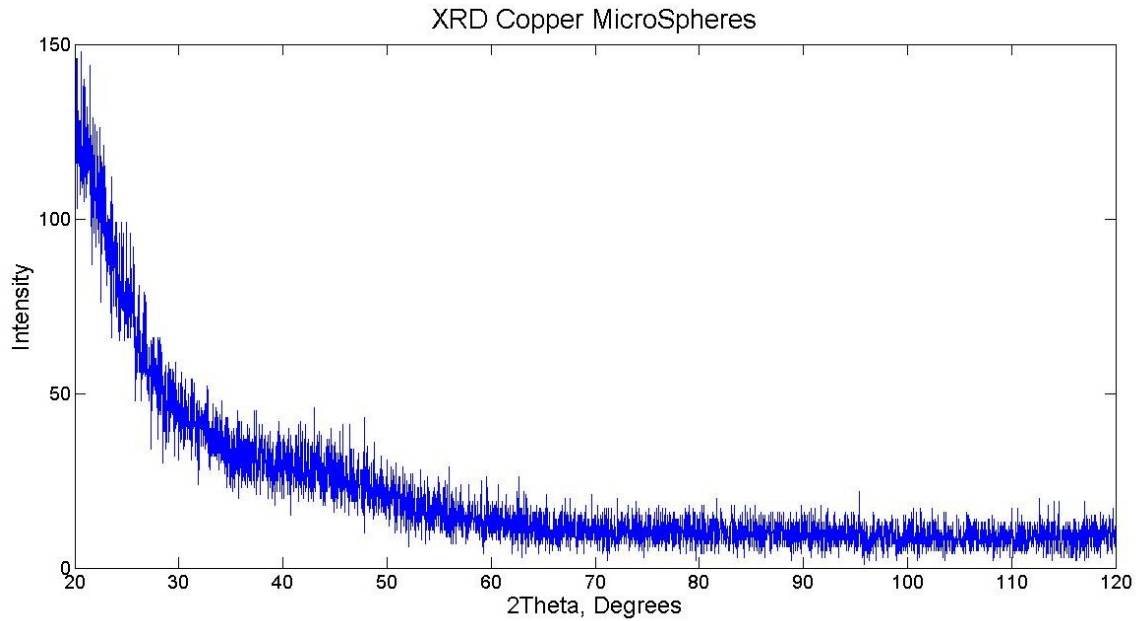
Figure 16: XRD data of sample Copper spheres. As can be seen in the spectrum, the copper spheres show no distinct peaks, therefore are said to be non-crystalline. The large slope at the lower end of the x-scale is attributed to geometry of the data collection device (See Figure 10), specifically the reflected X-Rays from the sample surface into the detector at low 2θ. XRD data courtesy of Dr. Kent Averett, AFRL/RX.

Pure cubic copper has the lattice structure of FCC (face centered cubic); the expected XRD spectra of copper with this crystalline structure can be seen in Figure 17. Expected peaks should occur at the positions shown in Figure 17 for the expected dominant oxide layer, Cu_2O [22]. Future research could include an investigation into FCC copper spheres; this could potentially lead to drastically different mechanical and electrical behavior. If the results showed a crystalline structure, similar to Figure 17, we would be able to use Bragg's law as mentioned in Chapter 2 in concordance with the XRD peaks to verify FCC copper was present.
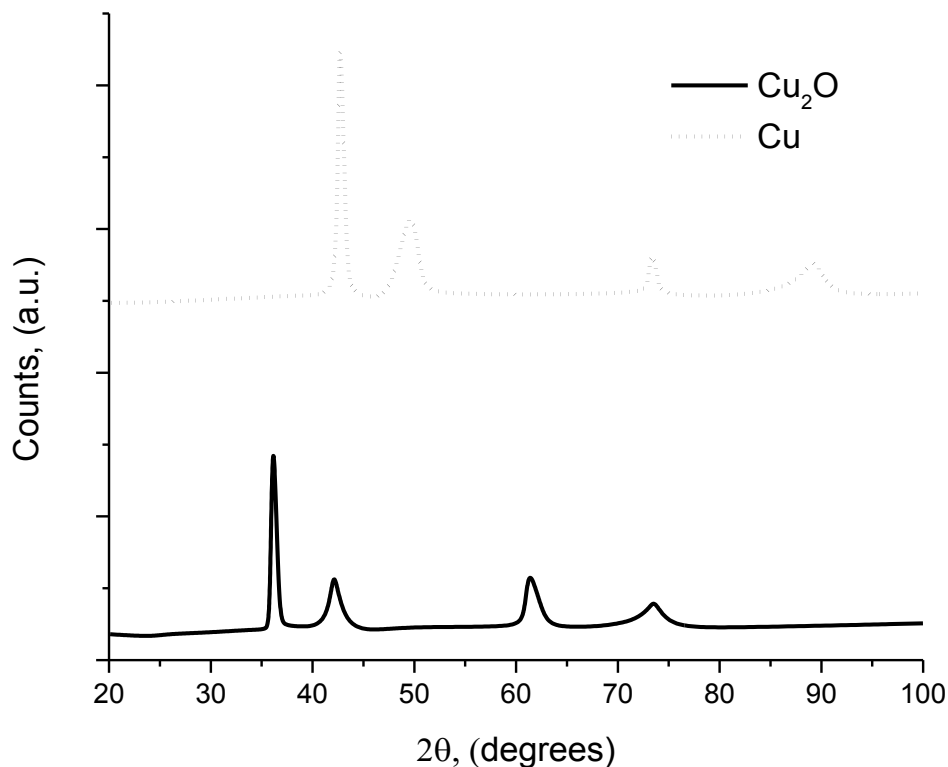
Figure 17: Cuprous Oxide (Cu_2O) and Copper (Cu) X-Ray Diffraction peaks of face centered cubic structure. With comparison to Figure 16, the relevant peaks are obviously not present on the Copper micro-spheres. This comparison further enhances the understanding that the spheres are of an amorphous lattice structure. Figure data from [22].

Nano-indentation

Henrich Hertz equations for elastic contact mechanics for spheres were applied to understand the sphere-sphere contact under compressive force. This deformation will provide a representative understanding with respect to deformation of the sphere to later compare with compression values applied to the sphere. Many tabulated values for elastic modulus and yield strength of copper assume an annealed sample, to be sure of the amorphous copper properties, nano-indentation had been pursued. Approximately 900 spheres were then mounted in Struers Polyfast mouting medium and polished down to a

42

minimum of 50nm slurry, which results in a similar surface roughness. Figure 18 shows

the polished cross sections following the 50nm slurry polishing.
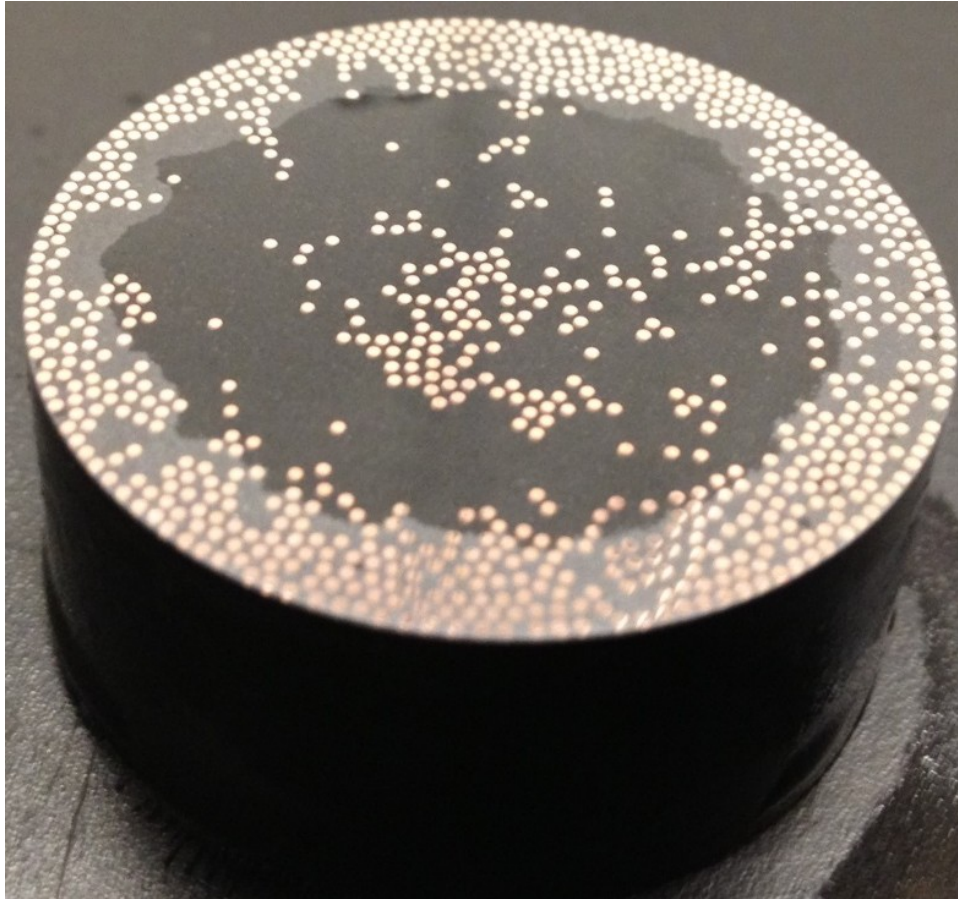
Figure 18: Approximately 900 'as received' copper spheres mounted in Struers Polyfast, and polished down to a 50nm surface. The necessity of a flat surface for nano-indentation is crucial for quality results.

Nano-indentation was completed on the polished cross section of one sphere with

an Agilent nano-indentation system, and data processed in concordance with ASTM

E2546 [3]. For this analysis a Berkovich tip was used, the geometry of the tip is well

defined (shown in Figure 19), as well as the material of the tip (diamond), therefore

solving for a resultant stiffness of the material being indented is possible. Berkovich and

Vickers indentation are similar in that the contact area with depth is the same between the

conical Vickers and the pyramid shape of the Berkovich [21].
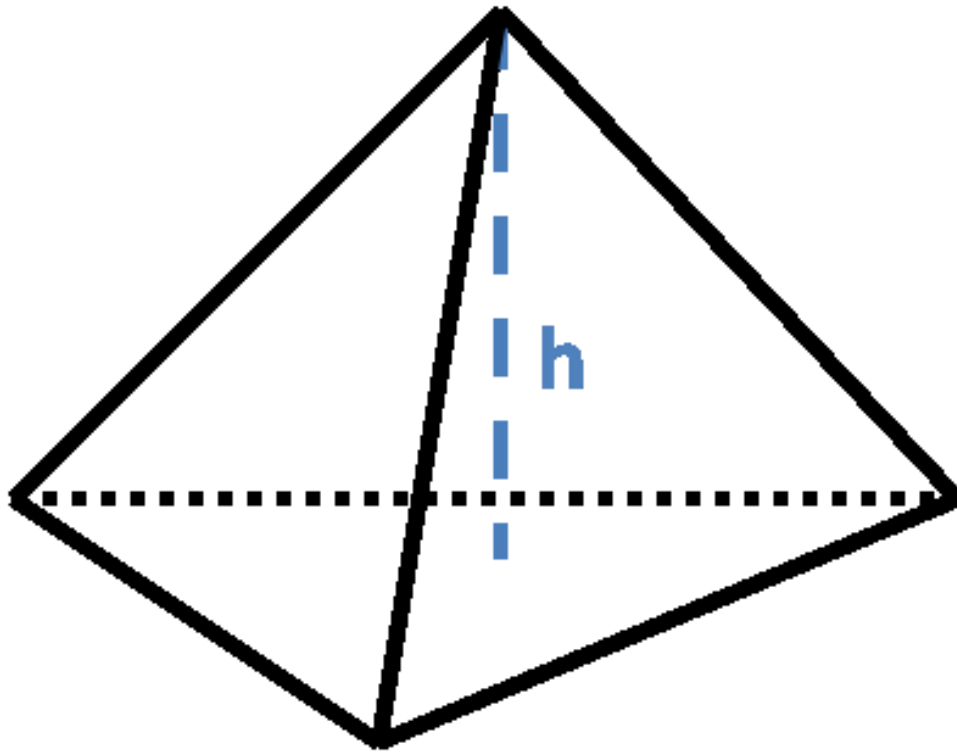
Figure 19: Berkovich nano-indentation tip. Knowing this h value along with the rest of
the tip geometry, a contact area can be found. The Berkovich tip was selected for its
simple relation to contact area, equation 17. Further dimensions can be found in [3].

The indenter was set to indent 1000nm into the material before holding and

unloading. Using images of the indentation sites, an analysis into the true depth was

carried out. An SEM image measuring the length of the 'legs' on the indentation site is

seen in Figure 20.
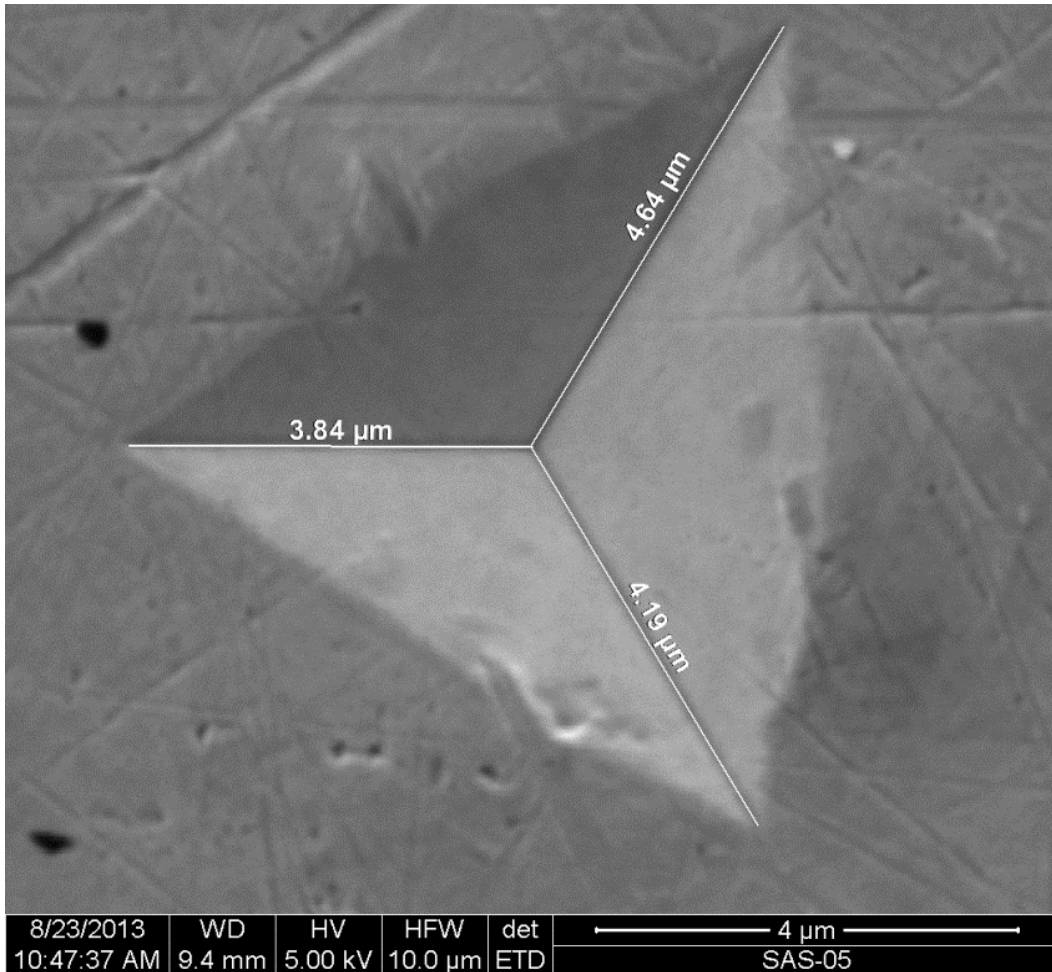
Figure 20: Shows a nano-indentation on the amorphous copper. To verify data from the Agilent G200 was accurate, measurements of each leg of the pyramid indentation were measured and the depth was calculated using an average of these, the shape of the tip and simple trigonometry. Calculated depth was determined to be approximately 960nm for this nano-indentation site. SEM image courtesy of Dr. Heath Misak AFIT/ENY.

The following figure shows the results of the nano-indentation measurement force versus loading data for 16 separate measurements on a single sphere. An Agilent G200 nano-indenter, along with ASTM E2546 was used to determine the elastic modulus of the copper material following the X-ray diffraction measurement.

Analyzing the unloading curve, 50% of the curve was chosen for fitting, resulting

in more conservative modulus translating to conservative inelastic deformation forces.

The resulting nano-indentation data is plotted in Figure 21 below.
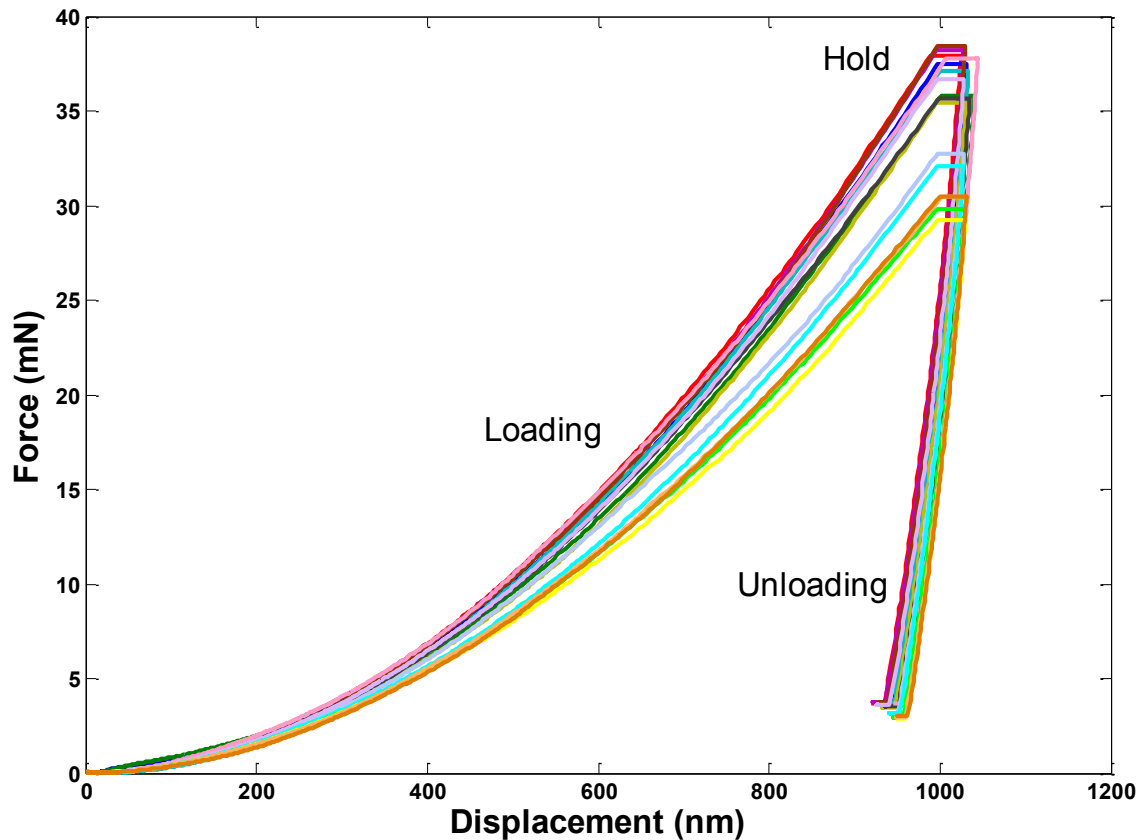
Figure 21: Nano-indentation data gathered with Dr. Heath Misak on a polished sphere
cross section. The unloading curve was then fit with conditions discussed in Chapter 2 to
find stiffness and eventually back out the elastic modulus of the material. The machine
begins be pressing the indentation tip into the sample surface in the loading phase,
followed by the holding and finally unloading phases. Nano-indentation data courtesy of
Dr. Heath Misak AFIT/ENY.

The resulting calculated modulus of the amorphous copper cross section was

found to be 106GPa. The hardness of the material was also determined, see equation 20

and *H* was determined to be 2.2GPa. Continuing with the hardness value, equation 19 was used to find approximate yield strength for the contact mechanic analysis; this value was found to be 729MPa. Figure 22 below shows the field of nano-indentation measurements on the single sphere.

Figure 22: SEM image of nano-indented cross section of 'as received' copper sphere sample. Few subsurface defects exist. Nano-indentation resulted in slightly lower Elastic modulus than polycrystalline sample as expected. SEM image courtesy of Dr. Heath Misak AFIT/ENY.

Using the new found information for yield strength, elastic modulus, and sphere diameter for the amorphous copper spheres, we can then look at what loading condition will cause the onset of inelastic deformation between sphere-sphere contacts. To do this, we u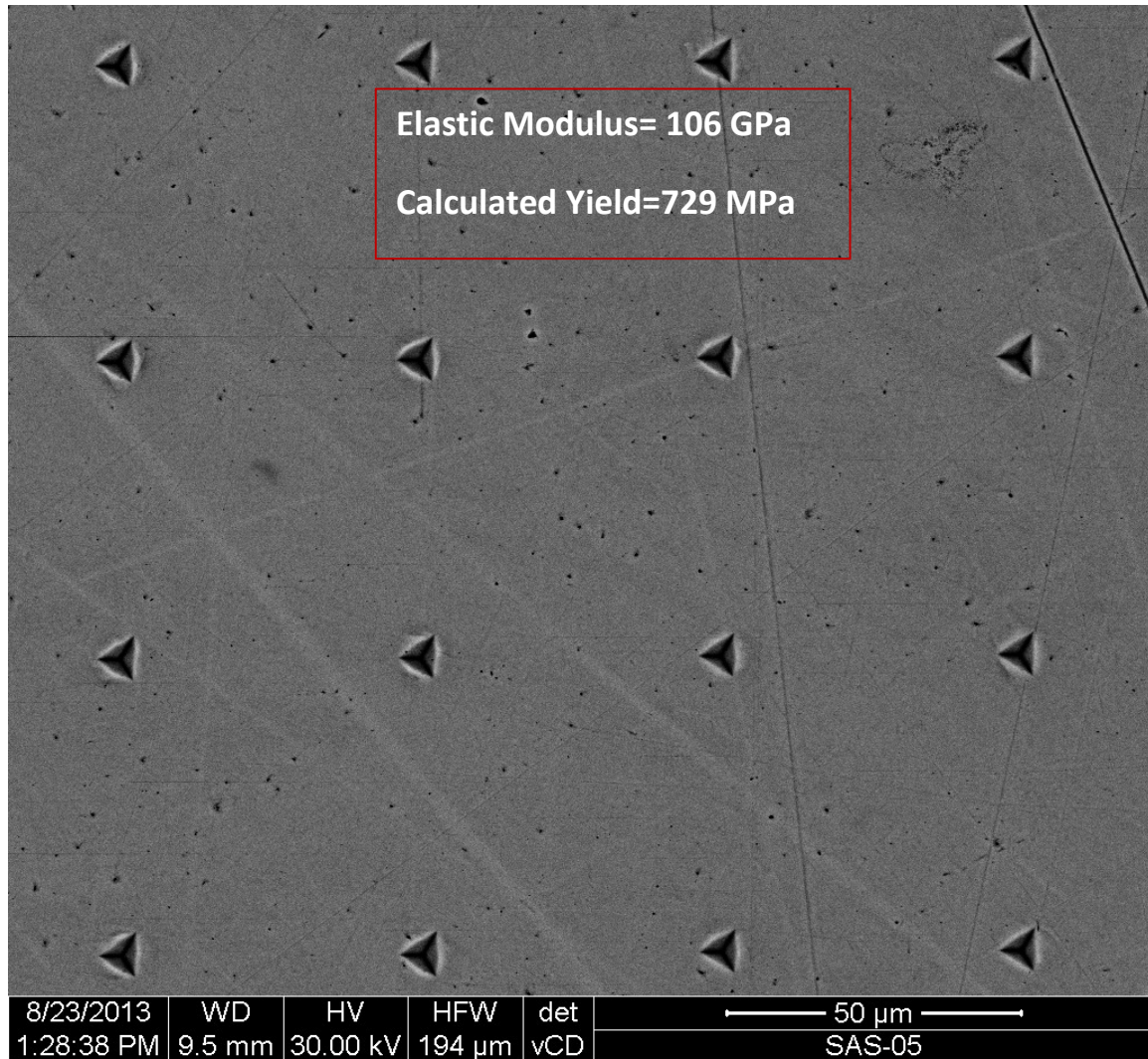se equations 3, 4, and the values found for yield and modulus in equation 7. Doing so, the value for E^*, assuming v=.3 (common v for metals) is found to be 58.24GPa and D is found to be 350μm. The force at first yielding of sphere-sphere contact is found to be about 300mN using the calculated yield and elastic modulus.

Since the difference in the calculated yield strength and the yield strength for annealed copper (69MPa, [31]) are so different, we can calculate the force at the initial inelastic yielding point for annealed copper. The modulus for the annealed case will be taken as 110GPa [31]. The resulting force value given the same D and v is much less at 233μN. A summary of the data can be found in Table 4 below.

Table 4: Summary of nano-indenter results and contact mechanics results where E^* is the reduced modulus between spheres, Y is the yield strength of the materials, F_Y is the loading at initial inelastic contact, and a is the radius of the contact at F_Y.

	E^* (GPa)	Y (MPa)	F_Y(mN)	a (μm)	Area (μm²)
Calculated	58.2	729.0	301.0	11.1	387.1
Annealed	60.4	69.0	0.233	1.004	3.166

X-Ray Photoelectron Spectroscopy

Surface conditions of the spheres as a whole are particularly important to understand so that a model can be applied to the MIM system. For further understanding of surface conditions on the sphere, X-Ray Photoelectron Spectroscopy was utilized. Unlike X-Ray Diffraction, this characterization practice takes into account only a small surface depth, making it a reasonable method to determine surface conditions. Most importantly, it must be noted that XPS is typically used on flat surfaced samples, this makes for accurate readings of the freed electrons, for the hemispherical surface which was looked at for the data to follow is expected not to return as many freed electrons as a flat sample would due to sample geometry.

The relevant peaks in binding energy for copper can be found at energies 933eV, labeled as $2p_{3/2}$ and 953eV, labeled as $2p_{1/2}$, while oxygen's O1s characteristic peak is found around 531eV [6]. Two data series were gathered before any argon sputtering occurred, in the higher energy levels, these two scans showed a minor trace of the 933eV copper peak, and at the lower energies the 531eV copper peak was dominant. Figure 23 shows the result of a sputter depth profile on a single sphere. Following the first sputter, the inverse was seen, large copper counts, and minor oxygen counts, this suggests a majority of the oxide was removed within the first sputter, and as seen in the plot as the sputtering progressed, the copper signal increased.

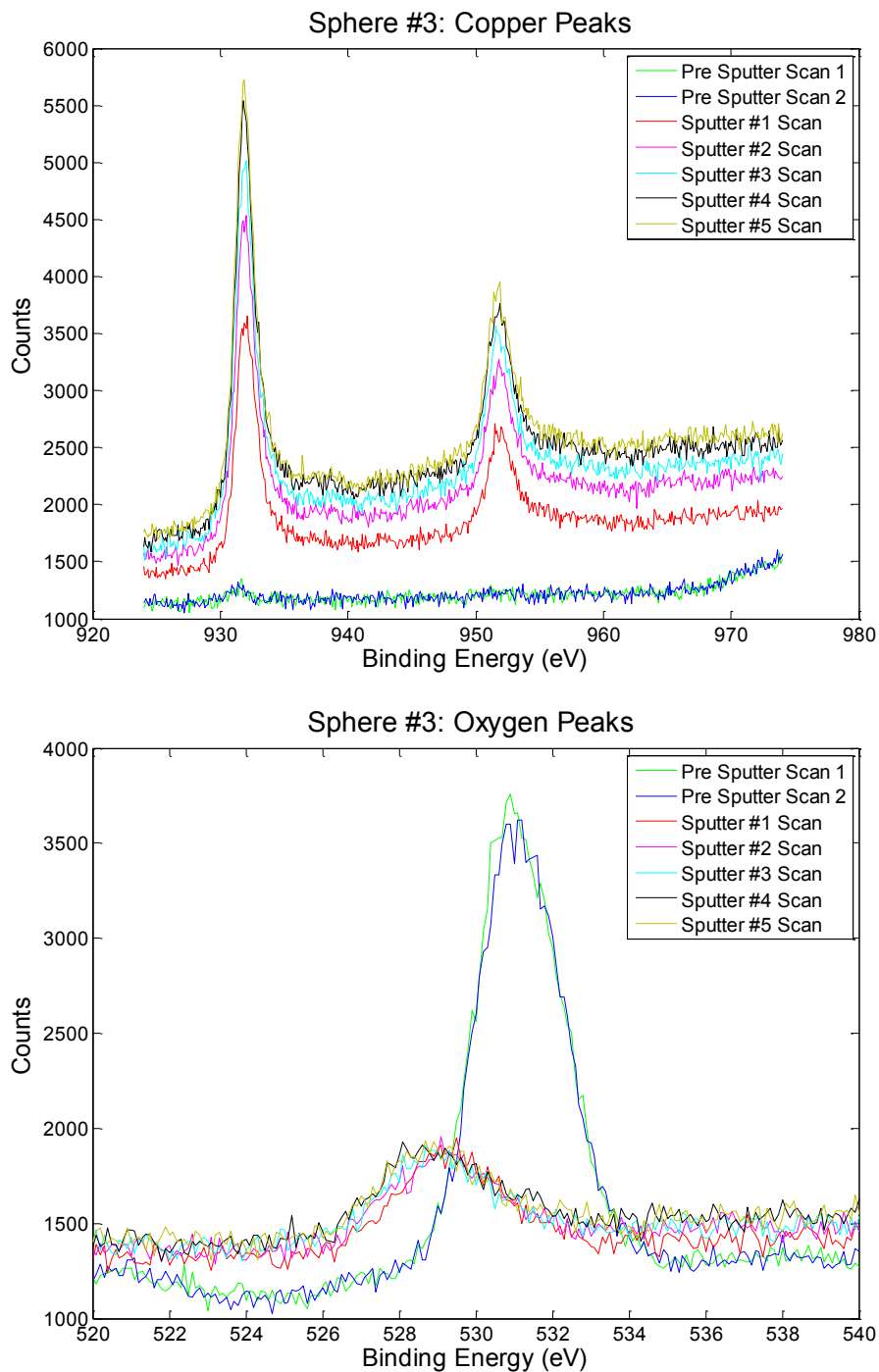Figure 23: X-Ray Photoelectron Spectroscopy Argon Sputter data for a randomly selected sphere surface. Oxygen is obviously present initially, post first sputter run, the oxygen is essentially completely gone, and only the two copper peaks remain. Oxygen peak in publication is described as 531eV, and Copper has distinct peaks and 933eV, and 953eV [6]. XPS data courtesy of Dr. Bruce 'Chip' Claflin AFRL/RYD.

The spheres appear to be covered by a surface of oxygen and possibly some other contaminant. If the surface was purely Cu_2O the values counts for copper would be twice the values for oxygen in an ideal planar sample. To remedy this surface inconsistency, various populations of spheres had been separated, etched, and re-oxidized. Acetic as well as nitric acids were both used as separate etching agents; nitric acid proved to be more reliable in experimental results. An open atmosphere hot plate and quartz tube furnace with controlled atmosphere were used to oxidize the spheres at various temperatures, the hot plate proved more reliable measurement results. The etchant/oxidation process for this thesis was carried out by Orta, and is discussed further in [14]. Successful combinations of etch and oxidation will be shown in Chapter 4.

Experimental Testing Device

The goal of this thesis is to compare the electrical properties and their dependence on mechanical compression in a single dimension array of spheres. With the information determined in this chapter, an apparatus for testing these properties simultaneously was designed. The apparatus seen in Figure 24 below is meant to be as simple as possible while still providing relevant information. The capillary tube with fixed electrode in one end is filled with copper spheres and mounted on the fixed stage; following this step the tungsten cantilever-electrode connected to the motor driven stage is inserted into the tube. The stage is then zeroed to a position at which the spheres are barely touching, or just begin to pack in the tube.
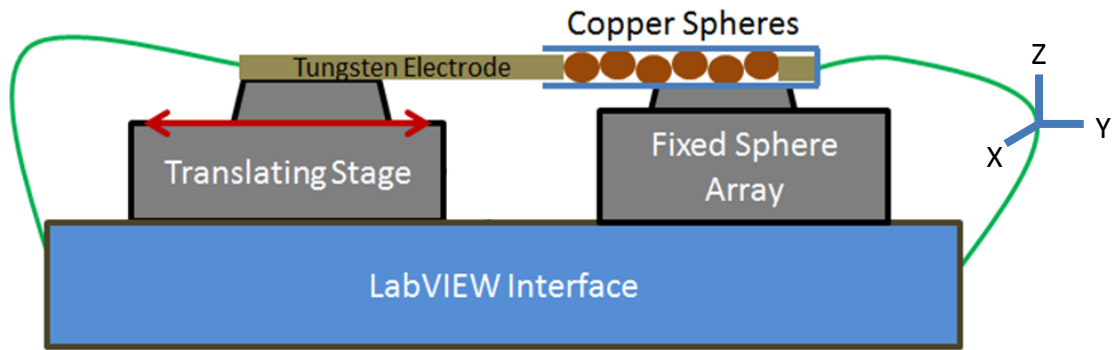
Figure 24: Shows representative experimental apparatus for 1-Dimensional sphere array. A Keithley 6517A system was controlled by LabVIEW software to take necessary electrical data.

With this testing apparatus, simultaneous mechanical and electrical measurements are made possible with an electrometer as well as the motorized stage controlled by a LabVIEW interface.

An example of an extreme compression is shown in Figure 25; the flat area is the result of inelastic deformation from sphere-sphere contact.
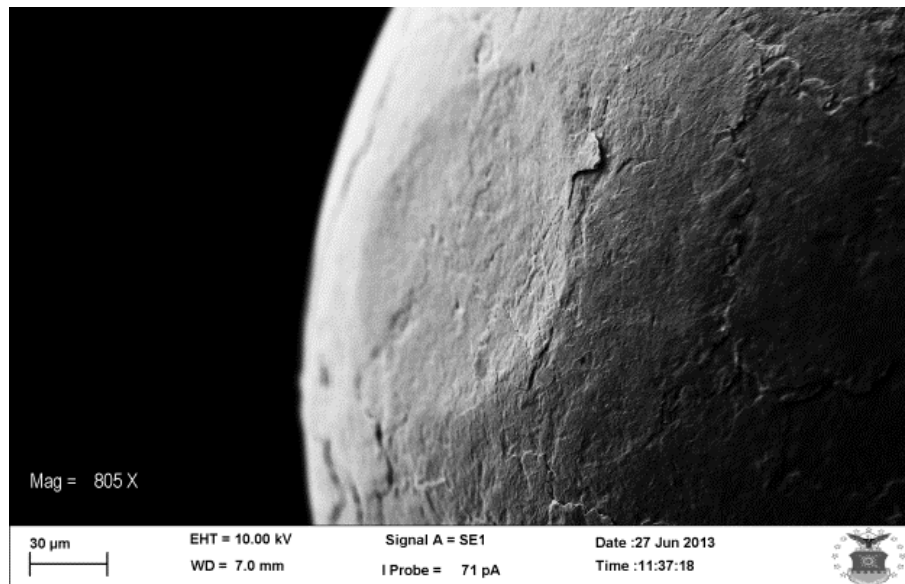
Figure 25: Upon excessive compressive loading on the copper spheres, permanent deformation occurs. SEM image courtesy of Dr. Daniel Felker AFIT/ENV.

This testing apparatus contains the spheres in a capillary tube with an inner diameter slightly larger than the sphere diameter; these values are about 838μm and 710μm respectively. The capillary tube is fixed on an adjustable stage, constrained internally by a tungsten rod. Figure 26 below shows a more detailed view of the testing device. The leads from the testing device (Keithley 6517a electrometer) contact the copper spheres through the conductive tungsten electrodes from Midwest Tungsten Supply. High purity (99.99%) tungsten was chosen from Midwest Tungsten Supply for its well defined low resistivity and high elastic modulus, 5.6e-6Ω-cm, and 400GPa respectively [19]. On an adjacent translating stage, a free tungsten cantilever electrode is used to apply various forces to the sphere array while simultaneously biasing. These forces are measured in the elastic region of bending in the tungsten electrode. This bench test device allows the user to exploit various combinations of mechanically compressing and electrically biasing the array with reasonable certainty of both electrical and mechanical measurements.
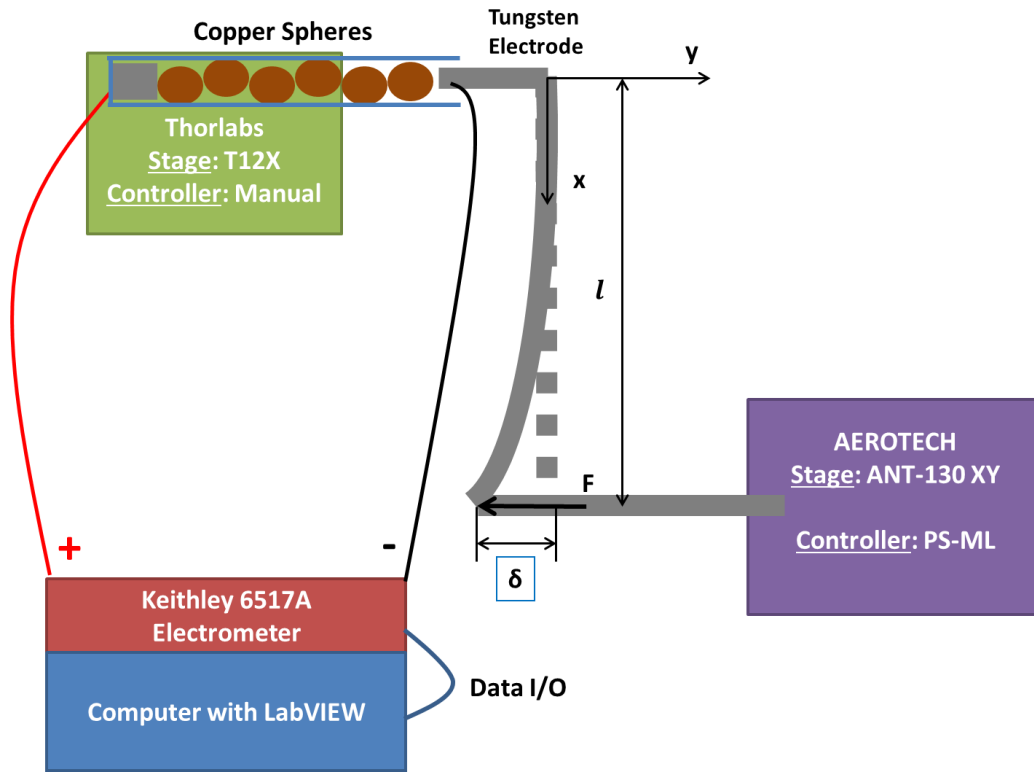
Figure 26: This figure shows a more detailed image top view of the stage setup from Figure 24. The cantilevered tungsten in addition to the motor-controlled stage allows for the force measurement discussed in Chapter 2. On the left side of the copper sphere array is a fixed tungsten electrode, the cantilever presses the sphere array against the fixed electrode while simultaneously measuring electrical properties.

Since the average sphere diameter is around 710μm, while the average tube inner diameter is 838μm some correction for error in force measurement can be accounted for due to the sphere packing inside the capillary tube. Figure 27 shows a representative area to scale containing a particle with ideal and unfavorable packing conditions shown. If stage is aligned properly, the maximum error in force measurement is 2.6mN/interface. For example, looking at a tube with three spheres, the initial value of force by the cantilever method must be subtracted by (2 interfaces and 2.6mN/interface), leaving a

54

correctable error of 5.2mN extra on force readout. The forces applied in this thesis were much greater than this 2.6mN, sometimes upwards of 500mN were applied, 4 and 8 sphere arrays were analyzed. Within a 4 and 8 sphere array, correction amounts to 7.8 and 18.2 mN respectively.
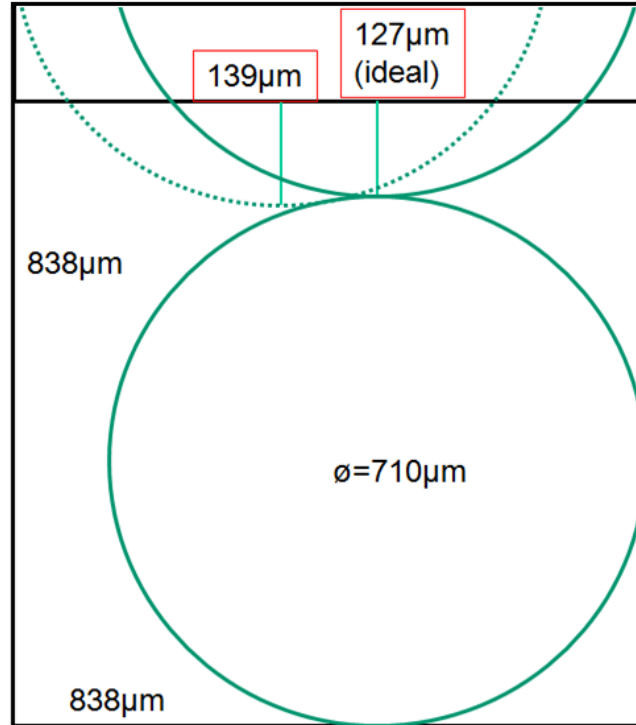
Figure 27: A sample area of 838μm by 838μm can be looked at as an area within the borosilicate capillary tube of diameter 838μm. Inserting a sphere of diameter determined as the average for the population (710μm), it can be seen that the packing difference (from the square reference area) is between 139μm and 127μm, a total of about 12μm. Applying this error to the conversion from cantilever displacement, it can be seen that for the current configuration of the apparatus, 2.6mN/interface is the error.

Holding a constant bias and varying force resulted in describing the pressure effect on carrier transport within the array. Variable bias during constant forces would describe current response with various area/load conditions, possibly leading to further

clues as to the true carrier and mechanism of transportation. Other conditions such as

variable force and variable bias, variable temperature, and frequency dependence will

also be considered in the future. Data collection is comprised of seven main tasks to

ensure repeatable data and can be found in Table 5 below.

Table 5: Process to successfully complete experiment on jammed granular copper array

1. Decide whether both voltage, force, or neither shall be the variable
2. Select number and type of sphere for experiment
3. Load spheres to capillary tube, fix tube on stage
4. Zero stage in X and Z so that electrode moves freely in/out of tube
5. Zero Y stage at first visual indication of contact
6. Constrain all axes
7. Proceed with measurement method chosen in 1.

Overview

Chapter 3 consisted of a complete explanation into the testing apparatus as well as

possible response of a granular memristive array. As a result of finding the copper

spheres to hold no periodic crystallinity, new values for the elastic modulus and

compressive yield strength were found to apply to contact mechanic equations. In

addition, surface measurements of 'as received' spheres led to appropriate etch and re-

oxidation steps to result in consistent electrical measurements. In Chapter 4 results from

various testing methods will be looked at and in Chapter 5, conclusions will be discussed

and applied to the system protection device this sensor array will ultimately be

incorporated in.

IV. Results and Analysis

The discussion section will begin with some measurements of a conductive breakdown across the oxide, replacing nonlinear behavior with ohmic behavior and how force affects this. We will continue on to a similarity in which Hertz contact mechanics is applied before analyzing some constant voltage, active loading measurements. Finally we will look into the hysteretic behavior of jammed copper memristive arrays with varying forces.

Breakdown

As mentioned in Chapter 2, if the voltage is raised above a limit, ohmic conduction results. This is dependent on sphere surface preparation and number of spheres being tested; the contact will become ohmic regardless of loading condition if the voltage is high enough. This ohmic behavior is irreversible for that position of the sphere array, if the capillary tube is tapped; the low, ohmic resistance is reset to a high, nonlinear resistance state. The tap is thought to adjust spheres to new surfaces, thus allowing for 'fresh' oxide at the contact. This characteristic was observed over various loading conditions and various etch/oxidation combination spheres, as was seen by Branly.

Using a nitric acid etch and 15 minute (min.) hot plate oxidized sphere array consisting of four spheres we can see an example of this force dependent shift in breakdown in Figure 28 below. In this figure as the voltage is swept for various force conditions while current is measured, we see an earlier 'bending' of the nonlinear IV trace. This figure also shows that as force increases, less voltage is required before

breakdown; this behavior was consistent throughout all surface conditions providing a nonlinear response.
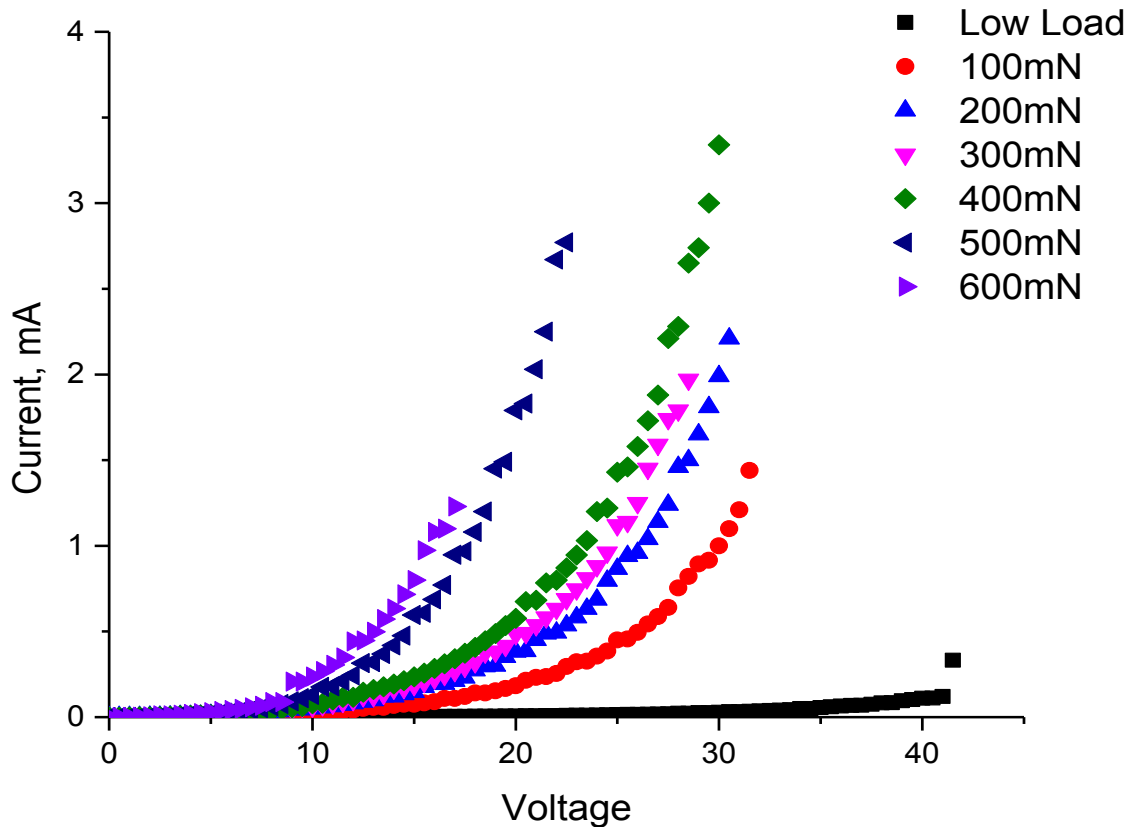
Figure 28: Voltage versus current for various loading conditions in a 4 sphere array. This figure shows that as force increases, less voltage is required to complete the breakdown of nonlinear conduction (shown by the abrupt stop in the curves).

Surface/Force Dependent Breakdown

Figure 29 below shows a comparison in static load versus the voltage required to breakdown nonlinear conduction. The surface conditions tested were the nitric etched, 1 and 15min. oxidations, along with the 'as received' with 5min. oxidation. The 1min. etch

samples turned out to be very sensitive with respect to the 15min. etch and 5min. no etch samples. Further investigations were carried out with the 5min. and 15min. samples, with the hope of a large contrast in measurements across the loading range. Figure 29 shows a summary of the breakdown comparison. The 1min. spheres resulted in ohmic contact with more than 100mN applied.

Figure 29: The plot above shows the breakdown voltages as a function of loading across the various oxidation/etching states in 4 sphere arrays. Evaluating this plot, it can be suggested that the 5min. no oxidation spheres are much more sensitive over this compression range than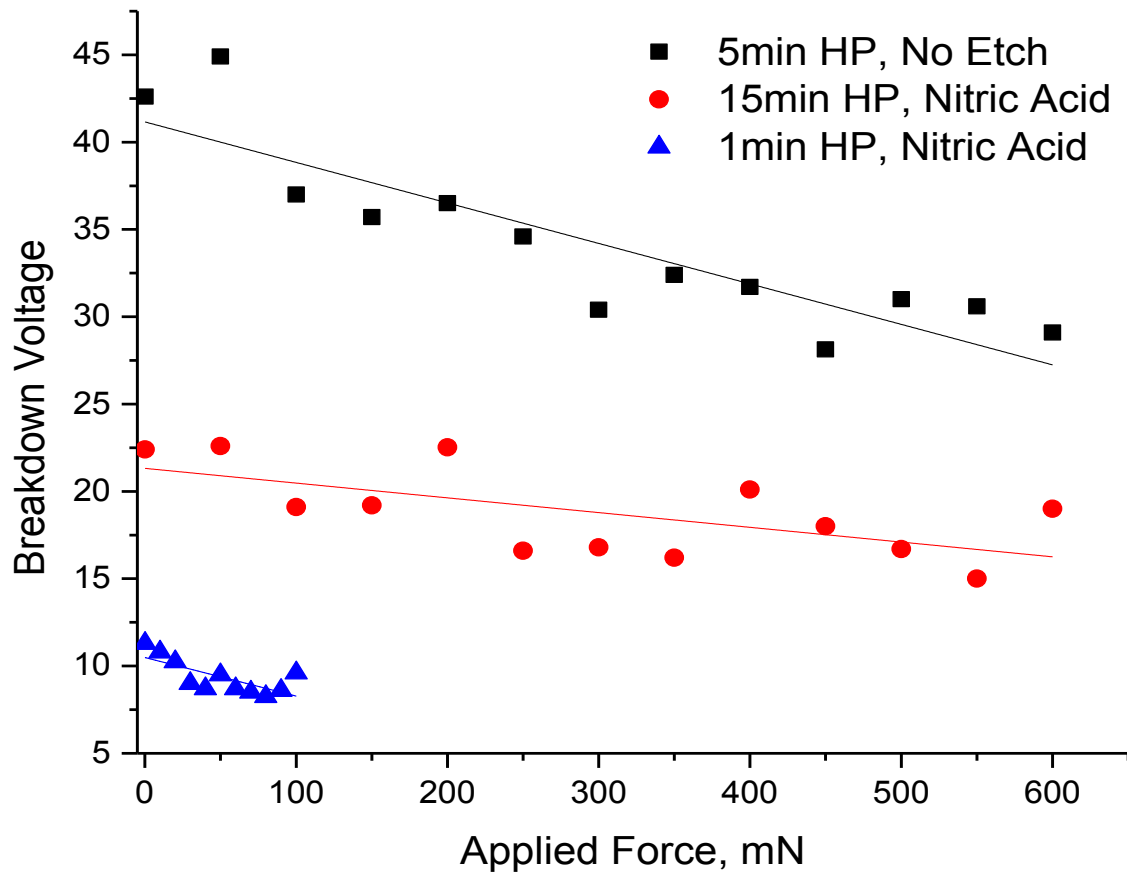 the 15min. oxidation due to the higher negative slope, and the 1min. oxidation, nitric etch spheres show purely ohmic contact after 100mN.

Array Size/Force Breakdown Dependence

Further investigations with the 15min. sample data were carried out under the assumption of repeatability being much greater than 'as received' samples, and having a larger measurable force range than the 1min. samples. Different experimental conditions tested with these samples consisted of a comparison of the number of spheres as compared to compression effect on breakdown voltage. Currently the Keithley 6517a is limited to 100V maximum and from previous data gathered. Orta [14] showed a maximum of 10 Volts per sphere on the 5min oxidation on the 'as received' sample set. All etched/re-oxidized spheres showed values lower than this. For the experiment shown in Figure 30 below, a voltage was swept at various loading conditions until breakdown occurred. The breakdown voltage increases proportionally to the number of spheres at the no-loading condition; this is consistent with what Orta observed [14]. One additional feature was the increase in sensitivity, as seen by the slightly larger negative linear slope in the figure below.
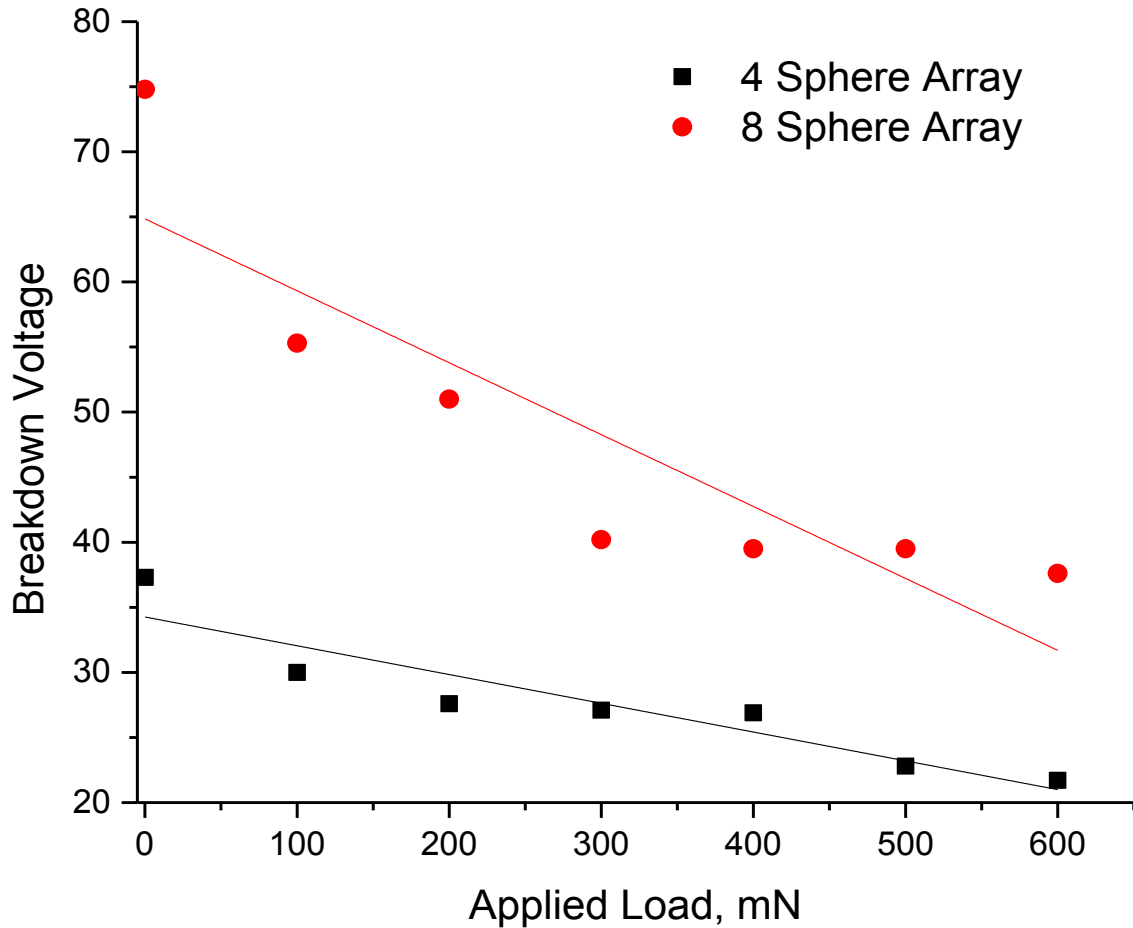
Figure 30: This plot shows additional data for the 15min. hot plate oxidation, Nitric Etch spheres. Comparing a single dimensional array of 4 spheres versus 8 spheres, this figure shows that an increase in spheres results in an increase in sensitivity to static compression. This shows a desired sensitivity to compression, but the voltages are relatively higher for the increased sensitivity. Linear functional relationships for each averaged data set as well. In this case for twice as many spheres (4v8), there are (N-1) sphere-sphere interfaces, therefore 3 for 4 spheres, and 7 for 8 spheres. The slopes seem to relate to a drop of about -7.63V/N/interface with a max error of 3.4%. Error bars represent ±10%

A summary of the linear relationships is shown below. It can be observed that once reduced to slope per interface the values are similar. Characterization of this property could be very helpful for design of an actual device, in that a breakdown in a

biased sphere array should result in an approximate force to cause that breakdown.

Further investigation into a pre-stressed sphere array could be seen as beneficial to the

system protection application. Just the opposite could be a configuration as well; the

breakdown with a preset loading condition on a known array size can result in the user

observing how much voltage was applied across the array.

Table 6: This table shows the difference in a linear functional relationship for 4 and 8
spheres. The slopes taken from Figure 30 with relation to the number of interfaces in the
array result in a relationship for voltage, force, and sphere array size.

	Intercept (V)	Slope (V/N)	Slope/Interface
4 Spheres	34.26	-22.11	-7.37
8 Spheres	64.85	-55.25	-7.89

Contact Area Size

As stated in Chapter 2, the resistance follows the $F^{-2/3}$ a sphere array. Shown in

the Figure 31 is the static loading against the maximum resistance, or R_{OFF}. The figure is

fitted with the resistance dropping with the -2/3 power of applied force. This agrees with

Hertz contact mechanics in concordance with the resistance in a wire at constant

resistivity, ρ.
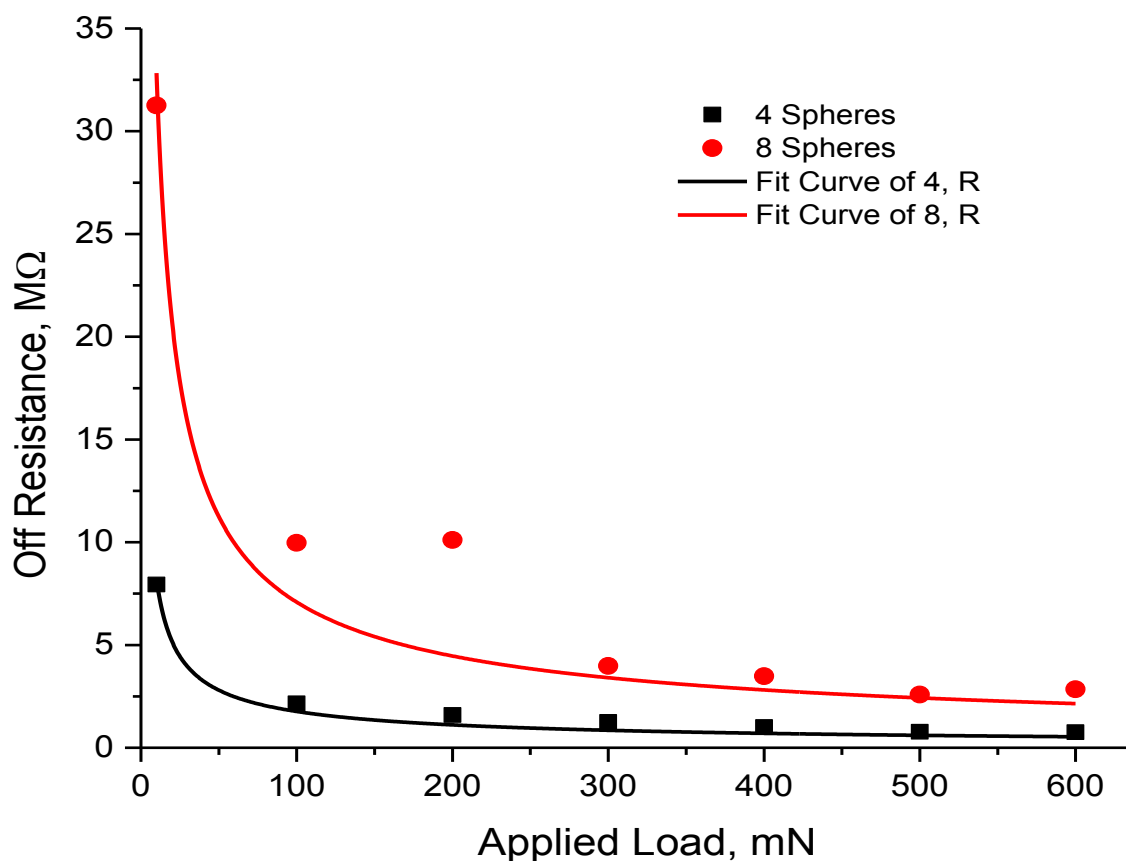
Figure 31: The plot seen here shows R_{OFF} values for 4 and 8 sphere arrays. When the power function discussed in Chapter 2 is applied, the result is above.

Active Loading Measurements

Ortas' relationship for breakdown of 'as received' spheres defined experimental constraints for future measurements. In the figure below, multiple voltages well below a breakdown voltage of 40V were used in active compression measurements on four 'as received' 5min. hot plate spheres. These plots show a time dependence on the loading-biasing combination. Figures 32 and 33 were taken while a constant bias was held over different loading rates. The 0.2mN/s rate is shown in Figure 32; this slower compression

rate may allow for more relaxation time, causing the breakdown at a lower load than the

increased rate in Figure 33 for the lower (magnitude) biased condition.
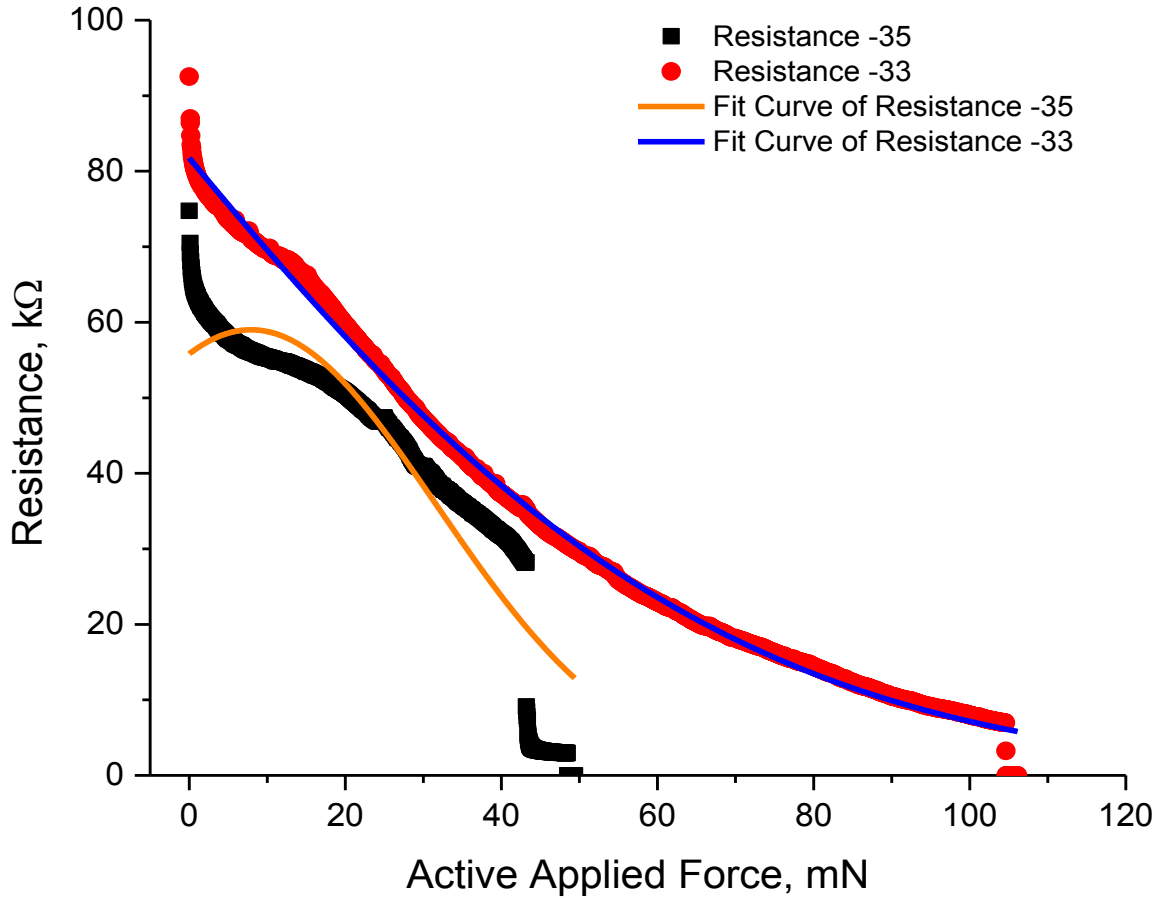
Figure 32: 0.2mN/s loading rate at different voltages. This figure compares different active loading rates and the resulting corresponding resistances. All decay data above follows a 2/3 decrease with force, this correlates well with the predictions using Hertz equations combined with resistance of an area. The best fit of the data is an exponential of a quadratic.

Figure 33 shows a loading at five times the rate of Figure 32. The lower applied

bias breakdown shows a similarity with the slower loading rate, at approximately 50mN.

While the higher (magnitude) applied bias broke down consistently throughout the two data sets.
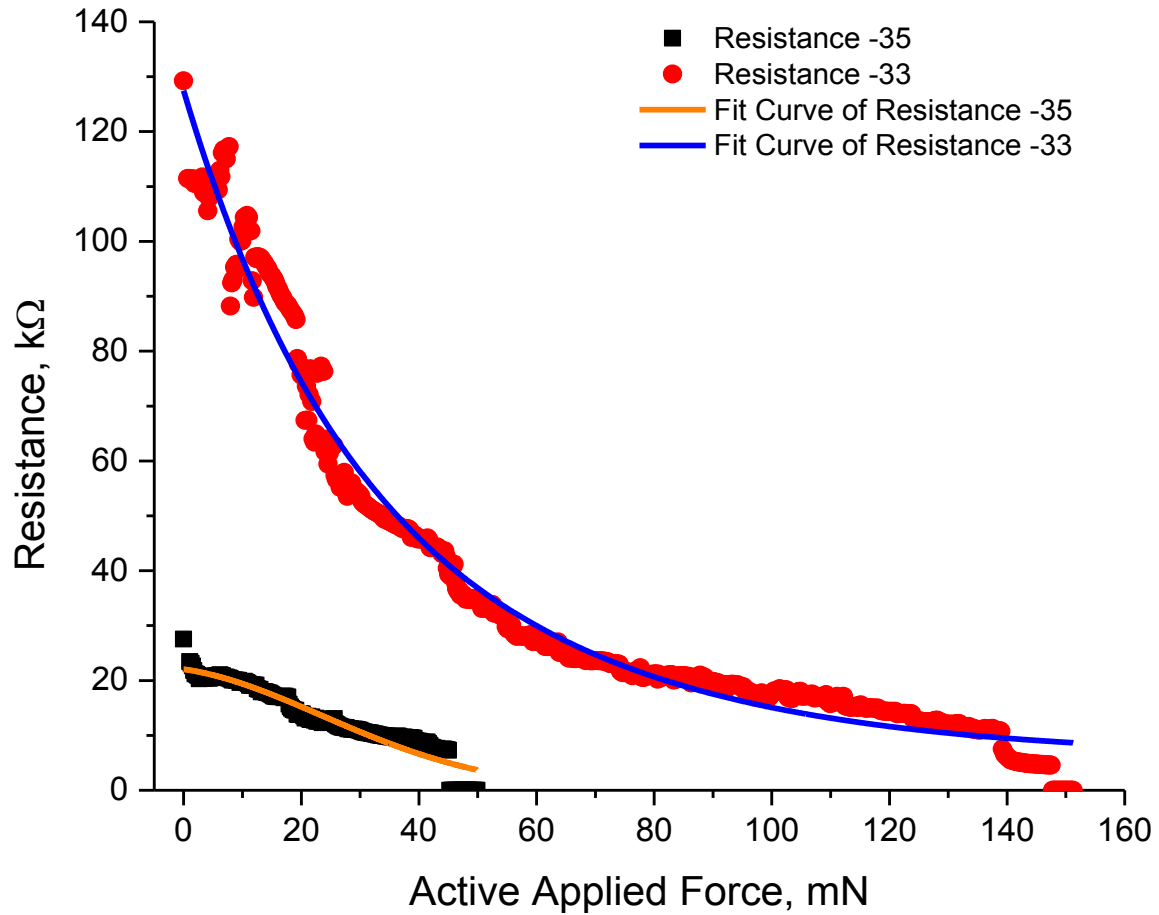
Figure 33: 1.1mN/s loading rate at constant -33 and -35 Voltages. The best fit of the data is an exponential of a quadratic.

Static Load and IV Sweep

As the compression force was increased, the shape and slopes of the IV traces shifted in a counter-clockwise manner, to lower resistance states. These lower resistance states gradually occurred at higher force states; this is obvious in most of the comparison

IV trace data. In Figure 34 below, four representative IV traces have been chosen to depict compression effects on IV response with different array sizes. At the unloaded state, both IV shapes seem to follow a somewhat linear relationship (plot is Sqrt(V) versus Log(I)), however when the force is increased, what looks to be the exponential as described by Schottky conduction . The change in overall slope should be a contribution from increased area or decreased oxide thickness between the contacts when the spheres are compressed. The overall change in shape is likely also a contribution of compression forces, but the actual mechanism is not yet known.
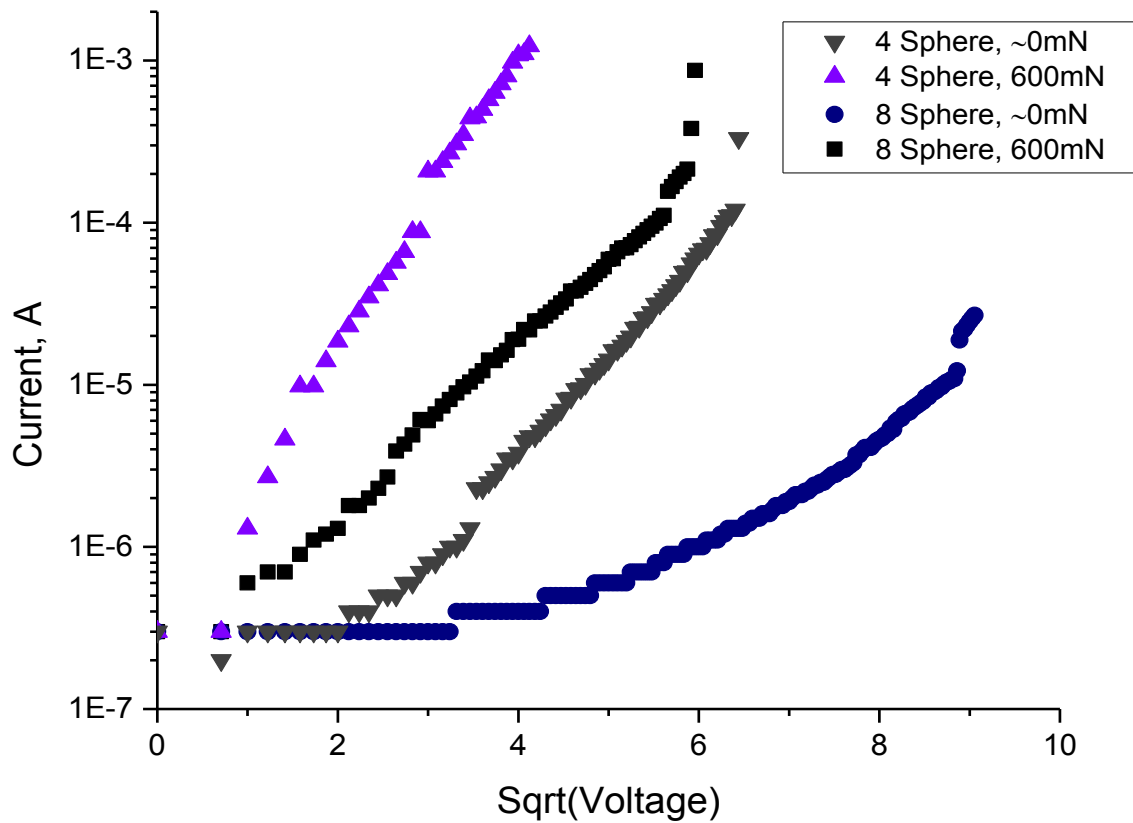
Figure 34: This plot shows log-current versus square root of voltage, to relate the voltage sweep to the Schottky conduction mechanism. This plot shows Schottky emission at higher contact loading.

Figure 35 below shows the result of a resistance-voltage trace. A sharp increase in resistance is seen at first until a critical voltage is hit, at which point a linear-exponential decay in resistance. Inevitably, a low enough resistance occurs (high enough current), resulting in breakdown. At higher loading conditions (low load, blue data; higher loading black data) the initial increase in resistance is not apparent, only the decay is present.
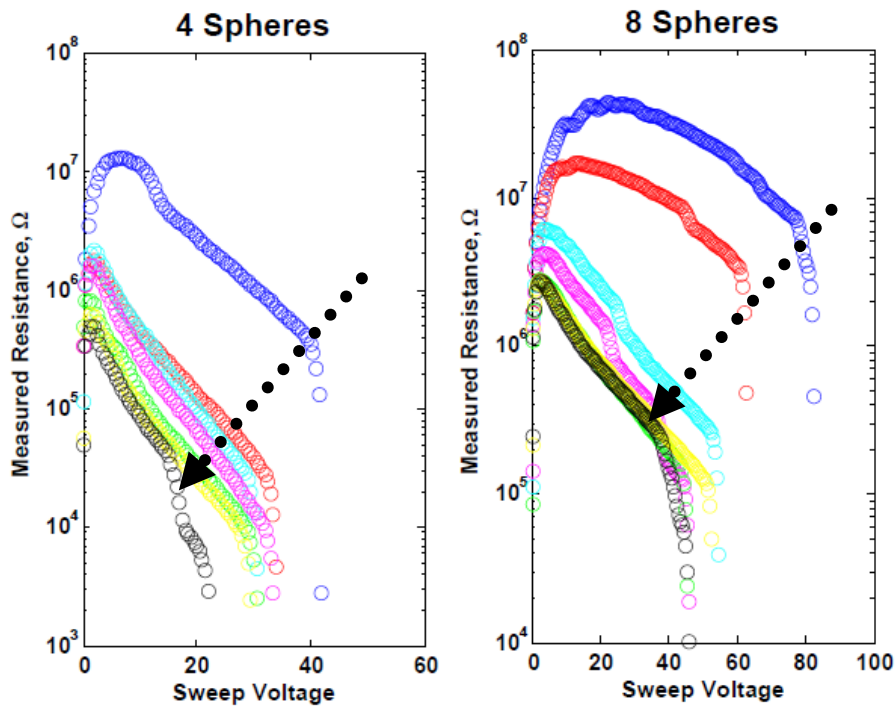
Figure 35: Evolution of Resistance-Voltage Measurements as static loading increases from a load near 0 to 600mN (following dashed line). Resistance of 4 and 8 sphere arrays made of 15min. hot plate oxidation process. As voltage is swept across the array a sharp increase in resistance is seen at lower voltages until a critical voltage is approached and a linear-exponential decay in resistance dominates. In the lower loading conditions, the decay is predominant with the resistance increase barely noticeable or not even present in some cases. Measurement data is terminated at ohmic breakdown.

Hysteretic Shift with Static Force

Hysteretic responses seen in the granular memristive system behaved similarly to Gale et al. With increasing contact area (force) the hysteresis loop showed shifting in the counter-clockwise direction, representing a shift to a lower resistance state. Figure 36 below shows representative data for the granular memristor system consisting of four spheres, each etched in nitric acid and oxidized on a hot plate for 15 minutes. For the following hysteretic loop, voltage was stepped up to a value known to be below breakdown voltage for four of these spheres, therefore keeping the voltage sweep regime within the nonlinear values. Once the voltage hit the predetermined value, 10V in this case, the voltage then steps back down to 0V the voltage would continue to -10V from there and back to 0V. As can be seen in Figure 36, the path is not the same in increasing bias as is decreasing in bias; this behavior is synonymous to memristive behavior.
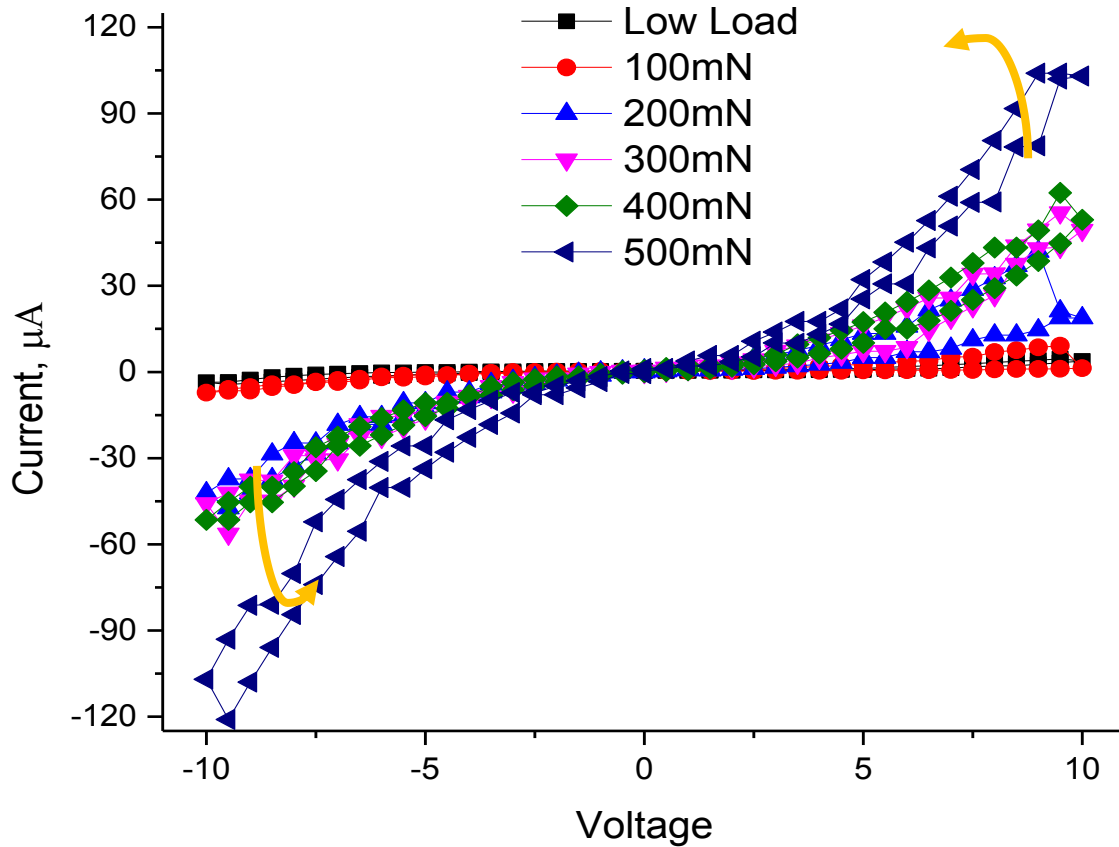
Figure 36: The hysteresis shift to lower resistance states for R_{ON} and R_{OFF} is seen with increasing contact area (increased loading on the sphere array). The spheres sampled for this set of data were four nitric etched spheres with 15 minutes of oxidation on a hot plate.

Overview

The information gathered in Chapter 4 shows us that there is dependence in the nonlinear voltage-current behavior on applied compressive force. This can be seen in reproducible hysteretic relationships as well as breakdown measurements. While observing breakdown with respect to applied force and number of particles, we can predict when a uniform surface condition array will breakdown knowing applied loading conditions.

V. Conclusions

The electrical responses to mechanical compressive loading have been observed in a memristive copper granular array sensor in this thesis. To conclude this work, final thoughts on the results section will be addressed. To close, an outline of future work for the purposes of this project will be discussed.

Summary

In Chapter 4, we saw a shift to lower resistance in the onset of possible Schottky voltage-current relationships with increasing compressive loading. This shifts to lower resistance states within hysteretic and breakdown measurements are thought to be due to increasing electric field or decreasing current density with increased compressive force. As was looked at in Chapter 1, compression between spheres should result in a thinner oxide and increased area of contact relating to increased electric field and decreased current density respectively. If this increased electric field reaches a value to dominate the dielectric properties of the oxide, possible breakdown is very well possible. Inversely, the increased contact area may provide more present defects in the oxide, possibly a thinner local oxide thickness allowing for current to flow across the oxide barrier and result in an earlier breakdown.

Falcons' original relation for the local contact temperature as found in equation 1 of this thesis was found to be more than 19,000K for four particles. This leads us to assume the local temperature relation breaks down for smaller spheres, and some material as well as geometric properties should be included to obtain a more reasonable value. Further investigations could be carried out to determine the feasibility of such relation.

Some similarities can be made with Falcons' experimental setup and although the results look similar it is quite the contrary. In Falcons' hysteresis loop, he showed a significant shift in the 'ON' portion with little change in the 'OFF' resistance. However we showed some shift in both 'OFF' and 'ON' states of our granular device.

Dearnaley et al. reports a similar behavior to Figure 34, 600mN curves in their unformed materials. Dearnaley goes to discuss Schottky contacts, which seem very likely to be responsible for the nonlinear behavior. Upon voltage application higher than threshold voltage for that device Dearnaley saw current increased by factors of magnitude, which were seen on the copper spheres as well [11].

For the characterization of a real world system protection device to allow the user to measure and/or observe the extent of unwanted intrusion to a device, this system is promising. As was seen in Figure 2, potential application to both passive and active monitoring devices are foreseeable. An adjustable sensitivity is possible with respect to surface conditions and preset loading conditions. A preset load could also potentially monitor compressive forces and any relaxation as well, in that with less force an increase in resistance results so long as the spheres aren't sufficiently past mechanical yield or electrical breakdown beforehand.

Future Work

Further experiments utilizing impedance spectroscopy across the array may provide more understanding of the conduction mechanisms. Impedance spectroscopy would ultimately lead to an explanation or verification of the nonlinear conduction mechanism present at various loading conditions. The most common form of Impedance

spectroscopy applies an AC signal and measures real and imaginary impedances, thus giving amplitude and phase shift. For purely resistive systems, this shift will be zero. Plotting the imaginary against the real results will produce results that will provide clues for the nature of charge transport in the metal-oxide-metal device.

In addition to impedance spectroscopy for a granular memristive device for system protection applications future work will include the expansion and characterization of 2-Dimensional planar devices, as well as 3-Dimensional volume devices. These will be tested with multiple types of spheres, some memristive, conductive, and possibly insulating in higher dimension devices. Multiple electrical outputs will also be utilized, setting various active and passive channels within a volume or planar device. Following a better understanding of how those systems work an investigation into how a device will respond to natural interference such as temperature, humidity, and possibly a nearby electric spark such as Branly had observed. Possible adjustment of Hertz contact theory to account for local adhesion of contacts may show a different relation in the local contact area as well as experiments with polycrystalline grains.

Figure 37 below shows the design contracted for a 2-Dimensional planar testing apparatus. The design consists of a recessed area with lid to constrain the spheres in one dimension, while allowing the application of force in the remaining two axial directions.

Figure 37: Design of 2D testing apparatus as contracted to Journey Electronics.
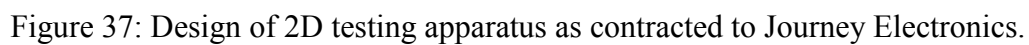
Appendix A: Cantilever

d=635μm (Diameter of Tungsten Cantilever)

l=35mm (Length of Tungsten Cantilever)

E=400GPa (Elastic Modulus of Tungsten Cantilever [19])

Where, $I = \frac{\pi d^4}{64}$

And, $F = \frac{y_{max} 3EI}{l^3}$

Therefore, $F = y_{max} *. 233 \left[\frac{N}{\mu m}\right]$

So movement of the Aerotech 130-XY stage 1000μm is assumed to bend the cantilever that far. The result is almost one quarter of a Newton of force applied to the sphere array. This force can be corrected using the method discussed on page 54 and 55 of this thesis.

Additional data available upon request, contact:

Dr. Alex G. Li AFIT/ENP

Gary A Willey Jr. AFIT/ENP

References

[1]   A. K. Jonscher, "Electronic Properties of Amorphous Dielectric Films.," *Thin Solid Films*, vol. 1, issue. 3, pp. 213–234, July 1967.

[2]   *Apple iOS CoreCrypto Module, v3.0 FIPS 140-2 Non-Proprietarty Security Policy,* FIPS_CORECRYPTO_IOS_US_SECPOL_01.06*, 2013*

[3]   *ASTM Standard Practice for Instrumented Indentation Testing*, ASTM E2546, 2007

[4]   B. Castle, "Memristive Properties of Thin Film Cuprous Oxide," M.S. thesis, AFIT/GMS/ENP/11-M01. Dept. Eng. Phys., Air Force Institute of Technology., WPAFB, OH, 2011. (ADA538757).

[5]   B. Lautrup, "Surface tension," in *Physics of Continuous Matter*, Benny Lautrup, 2010, pp. 69–94.

[6]   B. Vincent Crist, *Handbooks of Monochromatic XPS Spectra Volume 1 - The Elements and Native Oxides*, vol. 1. Wiley, 1999.

[7]   D. B. Strukov, G. S. Snider, D. R. Stewart, and R. S. Williams, "The missing memristor found.," *Nature*, vol. 453, no. 7191, pp. 80–3, May 2008.

[8]   E. Falcon, B. Castaing, and M. Creyssels, "Nonlinear electrical conductivity in a 1D granular medium," *The European Physical Journal B*, vol. 38, no. 3, pp. 475–483, Apr. 2004.

[9]   E. Gale, B. de Lacy Costello, and A. Adamatzky, "The effect of electrode size on memristor properties: An experimental and theoretical study," *2012 IEEE International Conference on Electronics Design, Systems and Applications (ICEDSA)*, pp. 80–85, Nov. 2012.

[10]   *FIPS 140-2 Cryptographic Module Security Policy*, IDCore30, 2013.

[11]   G. Dearnaley, "Electrical phenomena in amorphous oxide films," *Reports on Progress in Physics*, vol. 33, pp. 1129–1191, 1970.

[12]   "Industrial Tectonics Inc." (n.d.) http://itiball.com/copper_balls.php

[13]   J.-M. Dilhac and (Universite De Toulouse), "Edouard Branly, the Coherer, and the Branly Effect," *IEEE Communications Magazine*, no. September, 2009.

[14]   J. P. Orta, "Electrical Characterization of Spherical Copper Oxide Memristive Sensor Arrays," M.S. thesis, Dept. Elect. Eng., Air Force Institute of Technology., WPAFB, OH, 2014. (ADA)

[15]   K. Johnson, *Contact mechanics*, First Paper. New York: Press Syndicate of The University of Cambridge, 1987.

[16]   L. Chua, "Memristor-the missing circuit element," *Circuit Theory, IEEE Transactions on*, vol. C, pp. 507–519, 1971.

[17]   Li, Alex, PhD, Provided by.

[18]   M. A. Meyers, A. Mishra, and D. J. Benson, "Mechanical properties of nanocrystalline materials," *Progress in Materials Science*, vol. 51, no. 4, pp. 427–556, May 2006.

[19]   "Material Property Data, Tungsten, W, (drawn wire)" (n.d.) http://matweb.com/search/DataSheet.aspx?MatGUID=37fde7152eb94e3dbcbde8e2ed c0a497&ckck=1

[20]   M. D. Pickett, G. Medeiros-Ribeiro, and R. S. Williams, "A scalable neuristor built with Mott memristors.," *Nature materials*, vol. 12, no. 2, pp. 114–7, Feb. 2013.

[21]   M. M. Yovanovich, "Micro and Macro Hardness Measurements , Correlations , and Contact Models," 2006, no. January, pp. 1–28.

[22]   M. Wei, , N. Lun, X. Ma, and S. Wen, "A simple solvothermal reduction route to copper and cuprous oxide," Materials Letters, Volume 61, Issues 11–12, May 2007, Pages 2147–2150.

[23]   M. Y. Nadeem, A. Javed, and M. F. Wasiq, "Electrical transport phenomenon in the lead bismuth borate glasses," pp. 280–282, 2008.

[24]   R. Anderson, "Nuclear Command and Control," in in *Security Engineering*, 2nd Ed., Wiley, 2008, pp. 415–432.

[25]   R. Anderson, "Physical Tamper Resistance," in in *Security Engineering*, 2nd Ed., Wiley, 2008, pp. 483–522.

[26]   R.G. Budynas and J.K. Nisbett, "Load and Stress Analysis," in *Shigleys Mechanical Engineering Design, 9*th ed. New York City USA: McGraw-Hill, 2011.

[27]   R. S. Muller, T. I. Kamins, and M. Chan, *Device Electronics for Integrated Circuits*, 3rd ed., New York, NY: John Wiley and Sons, Inc., 2003, pp.139-173.

[28]   *Security Requirements for Cryptographic Modules*, FIPS PUB 140-2, 2001

[29]   S. M. (Department of E. E. Sze, N. C. T. University, K. K. N. (Central L. Hsinchu, Taiwan), T. MVC (a subsidiary of ProMOS Technologies, and C. San Jose, *Physics of Semiconductor Devices*, Third Ed. Wiley, 2007, pp. 227–236.

[30]   S. Nakano, S. Yamaura, A. Kitano, M. Sato, S. Uchinashi, T. Hamada, N. Umesaki, H. Kimura, and A. Inoue, "X-ray Diffraction Study for Mg 4 Pd Crystalline and Amorphous Alloys Using Synchrotron Radiation," vol. 45, no. 11, pp. 3232–3234, 2004.

[31]   W. Callister and D. Rethwisch, *Materials Science And Engineering An Introduction*, Eighth. Wiley, 2010.

[32]   W. Ellenbroek, *Response of granular media near the jamming transition*. 2007.

[33]   W. Lu, "Memristors: Going active.," *Nature materials*, vol. 12, no. 2, pp. 93–4, Mar. 2013.

[34]   Y. Kim, S. J. Kelly, A. Morozovska, E. K. Rahani, E. Strelcov, E. Eliseev, S. Jesse, M. D. Biegalski, N. Balke, N. Benedek, D. Strukov, J. Aarts, I. Hwang, S. Oh, J. S. Choi, T. Choi, B. H. Park, V. B. Shenoy, P. Maksymovych, and S. V Kalinin, "Mechanical control of electroresistive switching.," *Nano letters*, vol. 13, no. 9, pp. 4068–74, Sep. 2013.

[35]   Y. S. Gong, C. Lee, and C. K. Yang, "Atomic force microscopy and Raman spectroscopy studies on the oxidation of Cu thin films," *Journal of Applied Physics*, vol. 77, no. 10, p. 5422, 1995.

[36]   Zens, Timothy W.C. Class Presentation, MATL 680, Materials Characterization. School of Systems and Logistics, Air Force Institute of Technology, Wright-Patterson AFB OH, Winter Quarter 2013.

Vita

Gary A. Willey Jr. graduated from Beavercreek High School in Beavercreek, Ohio in 2009. Following which, he entered undergraduate studies at the Wright State University in Dayton, Ohio where he earned a Bachelor of Science degree in Mechanical Engineering in December 2012. During his time at Wright State University, he was employed as a teaching aid, and shortly an intern for GE Aviation before taking a position for SOCHE at AFRL at Wright-Patterson AFB, OH.   While working as a student research assistant in the Raman Spectroscopy lab in the Sensors directorate for AFRL/RX, he was selected for the current Master's Degree Program in Materials Science in the Engineering Physics Department of the Graduate School of Engineering and Management at the Air Force Institute of Technology at Wright-Patterson AFB, OH.

REPORT DOCUMENTATION PAGE

Form Approved
OMB No. 0704–0188

The public reporting burden for this collection of information is estimated to average 1 hour per response, including the time for reviewing instructions, searching existing data sources, gathering and maintaining the data needed, and completing and reviewing the collection of information. Send comments regarding this burden estimate or any other aspect of this collection of information, including suggestions for reducing this burden to Department of Defense, Washington Headquarters Services, Directorate for Information Operations and Reports (0704–0188), 1215 Jefferson Davis Highway, Suite 1204, Arlington, VA 22202–4302. Respondents should be aware that notwithstanding any other provision of law, no person shall be subject to any penalty for failing to comply with a collection of information if it does not display a currently valid OMB control number. **PLEASE DO NOT RETURN YOUR FORM TO THE ABOVE ADDRESS.**

1. REPORT DATE (DD–MM–YYYY) 27-03-2014	2. REPORT TYPE Master's Thesis	3. DATES COVERED (From — To) Jan 2013- Mar 2014

4. TITLE AND SUBTITLE	5a. CONTRACT NUMBER
Memristive Responses of Jammed Granular Copper Array Sensors to Mechanical Stress	
	5b. GRANT NUMBER HDTRA14111143
	5c. PROGRAM ELEMENT NUMBER

6. AUTHOR(S)	5d. PROJECT NUMBER
Willey, Gary, A., Jr.	
	5e. TASK NUMBER
	5f. WORK UNIT NUMBER

7. PERFORMING ORGANIZATION NAME(S) AND ADDRESS(ES)	8. PERFORMING ORGANIZATION REPORT NUMBER
Air Force Institute of Technology Graduate School of 2950 Hobson Way WPAFB OH 45433-7765	AFIT-ENP-14-M-44

9. SPONSORING / MONITORING AGENCY NAME(S) AND ADDRESS(ES)	10. SPONSOR/MONITOR'S ACRONYM(S) DTRA
Defense Threat Reduction Agency Calvin Shipbaugh 8725 John J Kingman Rd #6201 Fort Belvoir, Virginia Calvin.Shipbaugh@dtra.mil	11. SPONSOR/MONITOR'S REPORT NUMBER(S)

12. DISTRIBUTION / AVAILABILITY STATEMENT
DISTRIBUTION STATEMENT A: APPROVED FOR PUBLIC RELEASE; DISTRIBUTION UNLIMITED.

13. SUPPLEMENTARY NOTES
This material is declared a work of the U.S. Government and is not subject to copyright protection in the United States. This material is declared a work of the U.S. Government and is not subject to copyright protection in the United States.

14. ABSTRACT
A granular memristive device with the end goal of creating a novel system protection device is introduced in a 1-Dimension array. The electromechanical network will lay the groundwork for future 2-Dimensional and 3-Dimensional devices for simultaneous protection from intrusion. Off the shelf copper spheres with diameter of $710 \pm 11 \mu m$ were found through nano-indentation measurements to have elastic modulus of 106GPa, and compressive yield strength of 729MPa, these spheres were prepared for test in a 1-Dimensional array device. The arrays' response to mechanical perturbations modeled by Hertz contact mechanics can be monitored by simultaneous electrical measurements across the multiple metal-insulator-metal junctions. A shift in the nonlinear IV trace behavior to lower resistance states is the result of increasing compressive forces. Additionally a relation of breakdown to ohmic conduction of the junctions is found to be -7.6 in units of Volts per Newton per Interface for a 15 minute thermally oxidized sample array of 4 spheres. This granular array can be preset and monitored retaining the ability to recognize mechanical or electrical interference. The ability to have multiple electromechanically characterized chains within a 3-Dimensional volume allows for a complex redundancy in the future system protection circuit.

15. SUBJECT TERMS
Protection, Memristor, Granular, Array, Sensor, Force, Jammed

16. SECURITY CLASSIFICATION OF:			17. LIMITATION OF ABSTRACT	18. NUMBER OF PAGES	19a. NAME OF RESPONSIBLE PERSON Major Timothy W.C. Zens, PhD. (ENP)
a. REPORT U	b. ABSTRACT U	c. THIS PAGE U	UU	91	19b. TELEPHONE NUMBER (Include Area Code) (937) 255-3636, x4695; timothy.zens@afit.edu